Influenza A virus liquid condensates can undergo pharmacological hardening

Temitope Akhigbe Etibor[1], Sindhuja Sridharan[2], Sílvia Vale-Costa[1], Daniela Brás[1], Isabelle Becher[2], Victor Mello[1], Filipe Ferreira[1], Marta Alenquer[1], Mikhail M Savitski[2] and Maria João Amorim[1,*]

[1] Cell Biology of Viral Infection Lab, Instituto Gulbenkian de Ciência, Oeiras, Portugal

[2] EMBL, Heidelberg, Germany

***** Corresponding author, mjamorim@igc.gulbenkian.pt

ABSTRACT

Multiple viral infections form biomolecular condensates in the host cell to facilitate viral replication[1]. Accumulating evidence indicates that these viral condensates rely on specific material properties for function [2], but how these properties may be altered efficiently remains vastly unknown. Here, we use influenza A virus liquid cytosolic condensates [3], A.K.A viral inclusions, to provide a proof of concept that stabilizing transient interactions among the interactome in IAV inclusions more efficiently hardens these structures than varying temperature or concentration both in *in situ* and in *in vivo* models. This stabilization can be achieved by drug targeting, inducing changes in the solubility of viral proteome without affecting host cellular proteome. Our work supports the development of antivirals targeting the material properties of biomolecular condensates in viral infections. It also provides a framework for the efficient selection of pharmacological compounds with this activity and thus provides an advance in disease therapy.

INTRODUCTION

Central to the spatiotemporal control of reactions in many viral infections is the formation of biomolecular condensates to facilitate key steps of viral lifecycles [1]. For influenza A virus (IAV), this is key for assembling its segmented genome, a complex composed of 8 different viral RNA segments (vRNA) [4]. Each vRNA is encapsidated by molecules of nucleoprotein (NP) along its length, with one unit of the RNA dependent RNA polymerase (RdRp, consisting of PB2, PB1 and PA) bound to the base-paired RNA termini, forming viral ribonucleoproteins (vRNPs) [5]. How the 8-vRNP complex self-assemble is unknown, although it is known that it relies on RNA-RNA interactions amid vRNPs and is a selective process because most virions contain exactly 8-different segments[6]. At a critical step of the IAV lifecycle, vRNPs induce the formation of cytosolic condensates, known as viral inclusions [7-12], which we postulated to be sites dedicated to IAV genome assembly[3]. Interestingly, IAV cytosolic inclusions exhibit liquid properties (fuse and divide, dissolve upon shock and are dynamic) [3], providing the first indication that defined material properties are critical for the formation of influenza epidemic and pandemic genomes.

As the list of viruses utilizing liquid biomolecular condensates is increasing fast, including reoviruses, human cytomegalovirus, HIV, rabies, measles, SARS-CoV-2 (reviewed in [1,13]), it becomes pertinent to ask whether targeting the material properties could constitute a novel antiviral approach. Supporting such potential, the Sonic hedgehog pathway antagonist cyclopamine and its analogue A3E were described as potent inhibitors of viral replication of human respiratory syncytial virus through altering the material property of viral condensates but exhibit off-target effects on other cellular condensates [14]. This lack of specificity was also reported for cancer therapies targeting biomolecular condensates [15]. Therefore, a critical advance in disease therapy targeting material properties of biological condensates not only has to define efficient strategies to modify the material properties but also ensure the selective delivery of compounds to these structures.

In this work, we meet the critical need to identify efficient strategies to harden IAV liquid inclusions. For this, we systematically assessed the impact of well-characterized thermodynamic variables on the material properties of biological condensates, including temperature, concentration and number/strength of ligations within the condensate interactome. We found that the stabilization of intersegment interactions most efficiently hardens IAV inclusions. Critically, we show that the hardening phenotype is observed in the lungs of infected mice. We also report that it is possible to affect viral inclusions without imposing new changes in protein abundance and solubility of

infected cells at the proteome-wide level. Our data support the development and provides a critical advance in disease therapy targeting the material properties of cellular condensates in viral infections.

RESULTS

The increase in strength of IAV interactions hardens liquid IAV inclusions.

We previously demonstrated that viral inclusions formed by IAV infection display a liquid profile in the sense that they drip, acquire a spherical shape upon fusion and dissolve in response to hypotonic shock or brefeldin A treatment [3]. Here, we assessed how to alter these properties. For this, we systematically probed the impact of temperature, concentration, and number of ligations on the material properties of liquid inclusions formed upon influenza A/Puerto Rico/8/34 (PR8) infection. We selected these parameters as they are well understood to regulate the interactions amongst components and the material properties in condensates [16,17]. Methodologically, we employed established protocols for altering the parameters and quantified the impact on the number, nucleation density ($\rho = \frac{number\ of\ inclusion}{Cytoplasm\ Area}$, μm^{-2}), size, shape, dynamics, supersaturation ($S = \ln \frac{Cdilute}{Csaturation}$), and the Gibbs free energy of partition (henceforth called free energy, ΔG) of viral inclusions using the analytical tools described in [16,18]. We reasoned that dramatic alterations in the material properties can be determined from significant shifts in ΔG. In thermodynamics, the change in free energy between two conditions ($\Delta G = -RT\ln K$) relates to the partition coefficient K ($K = \frac{Cdense}{Cdilute}$), which, in this case, is the ratio between the concentrations of vRNPs in IAV inclusions (C_{dense}) and outside the condensates (C_{dilute}). To determine the concentration, we used the mean fluorescence intensity (MFI) of NP as proxy of vRNP concentration [7,19], as it is well established that most cytosolic NP is in the form of vRNPs [7,8,10,12].

To assess the entropic contribution of free energy, we compared viral inclusions incubated at 4 º, 37 º and 42 ºC for 30 minutes at 8 hpi. Although this short duration in temperature changes is not expected to alter the levels of cytosolic vRNPs, we observed an increase in vRNP amount in the cytosol at 42 ºC (Fig. 1a), presumably because the antibody has more access to vRNPs dispersed rather than in inclusions. Importantly, the aspect ratio and circularity of viral inclusions did not change with temperature variations (Extended Data Fig. 1a-c). Comparing all conditions, higher temperatures (37º to 42ºC) led to a lower number (Fig. 1b, Extended Data Fig. 1d) of viral inclusions, with less vRNPs in condensates (C_{dense} decreases) (Fig. 1c,d, Extended Data Fig. 1a,e), and smaller sized inclusions (Extended Data Fig. 1f-h). Importantly, at these temperatures,

the structures were only modestly destabilized, as observed by an increase in Gibbs free energy (-3210 @ 37 ºC to -2297@ 42 ºC, mean, Fig. 1e,f, Supplementary Table 1). These alterations are consistent with heat disruption of molecular interactions leading to disassembly of IAV inclusions with temperature. Conversely, decreasing the temperature until 4ºC leads to bigger inclusions (shift in area from 0.14 ± 0.027 μm^2 at 37 ºC to 0.2 ± 0.03 at 4ºC, Extended Data Fig. 1a,h, Supplementary Table 1), containing more vRNPs per area (C_{dense} at 37ºC of 44.4±6.66 AU and at 4ºC of 63.2±6.40 AU, Supplementary Table 1) but does not significantly change the stability of IAV inclusions as determined by Gibbs free energy (Fig.1f).

Concentration of material is a key determinant for the physical properties of condensates [16,20,21]. Two factors were shown to drive the formation of IAV inclusions - vRNPs and Ras-related in brain 11a (Rab11a) [3,7,10,11,19,22]. In fact, vRNP accumulation in liquid viral inclusions, requires its association with Rab11a directly via the viral polymerase PB2 [7,22]. Therefore, we evaluated how concentration of the drivers impact behaviour of IAV inclusions. As it is well-established that the concentration of vRNPs increases in the cytosol with time of infection [23], we analysed viral inclusions over a time course. As the new vRNP pools are added to the cytosol (Fig. 1g), both the C_{dense} and C_{dilute} increase up to 12 hpi (Fig. 1h, Extended Data Fig. 2b-d), consistent with multicomponent biological systems [16]. As infection progresses, condensates augment in size but from 12 hpi plateaux, which is a sign of shape maturation, as seen by changes in aspect ratio (Extended Data Fig. 2h-i). Importantly, the density of condensates stabilizes from 12 hpi, accompanied by an increase in the diluted cytosolic phase, which indicates that the critical concentration occurs around 12 hpi and nucleation centres (ρ) decrease (Fig. 1h, Extended Data Fig. 1e,f). Viral inclusions maintain a liquid character since they can fuse and divide throughout (Fig. 1j, Extended Data Fig. 2n, Supplementary Video 1).

Next, to address the role of Rab11 concentration, we compared IAV inclusions in endogenous and overexpressing Rab11a (Rab11a-WT) at 8 hpi, which has the lowest ΔG. Rab11a overexpression did not alter the levels of cytosolic vRNPs (Fig. 1g, blue shaded area, comparative to 8 hpi), nor change in Gibbs free energy (Fig. 1i), or nucleation (Extended data Fig. 2e), but led to bigger viral inclusions (Extended Data Fig. 2h), containing more vRNPs (Extended Data Fig. 2d) that exhibited a liquid character with fusion and fission events taking place (Fig. 2j, Extended Data Fig. 2n, Supplementary Video 2). These data indicate that altering Rab11a and vRNP concentration mildly affects IAV inclusions' material properties.

Another critical regulator of condensates properties is how its components interact [2]. Therefore, we predict that oligomerizing vRNPs to each other or to Rab11a will change the viscoelasticity of condensates similar to iPOLYMER for intracellular hydrogels [24]. For IAV, it was shown that the

drug nucleozin has affinity and binds to different sites of the viral nucleoprotein (NP), operating as a pharmacological sticker that oligomerizes NP either free or on vRNPs [25-27]. To confirm the pharmacological sticker activity of nucleozin, we evaluated the thermal stability of vRNPs [28] by assessing the stability of the viral polymerases and not NP, given that the RdRp are part of vRNPs but not targeted directly by nucleozin. This avoids analysing effects of nucleozin on free NP. At 62ºC, the levels of PB2 are higher when nucleozin is present (Extended Data Fig. 3l,m), which means that nucleozin stabilizes vRNPs. Next, we tracked how nucleozin affected IAV liquid inclusions from 5 min to 2h after addition (Fig. 1k, Extended Data Fig. 3a). Nucleozin-treated inclusions were bigger, lost circularity and roundness (Extended Data Fig. 3b-d) and decreased in number (Fig. 1l, Extended Data Fig. 3e), suggesting that they were stiffer. Importantly, these structures were energetically more stable, with lower free energy (from -1448 $cal.mol^{-1}$ at 8 hpi to -5037 $cal.mol^{-1}$ after 2 h post nucleozin, Fig. 1m-o, Extended Data Fig 3f-h, Supplementary Table 1), and absorbed cytosolic vRNPs, as C_{dilute} decreased (Fig. 1m,p, Extended Data Fig. 3f-h). Together, the data suggest that stabilizing vRNP interactions changes inclusions (Extended Data Fig. 3k) more efficiently than the other strategies tested above.

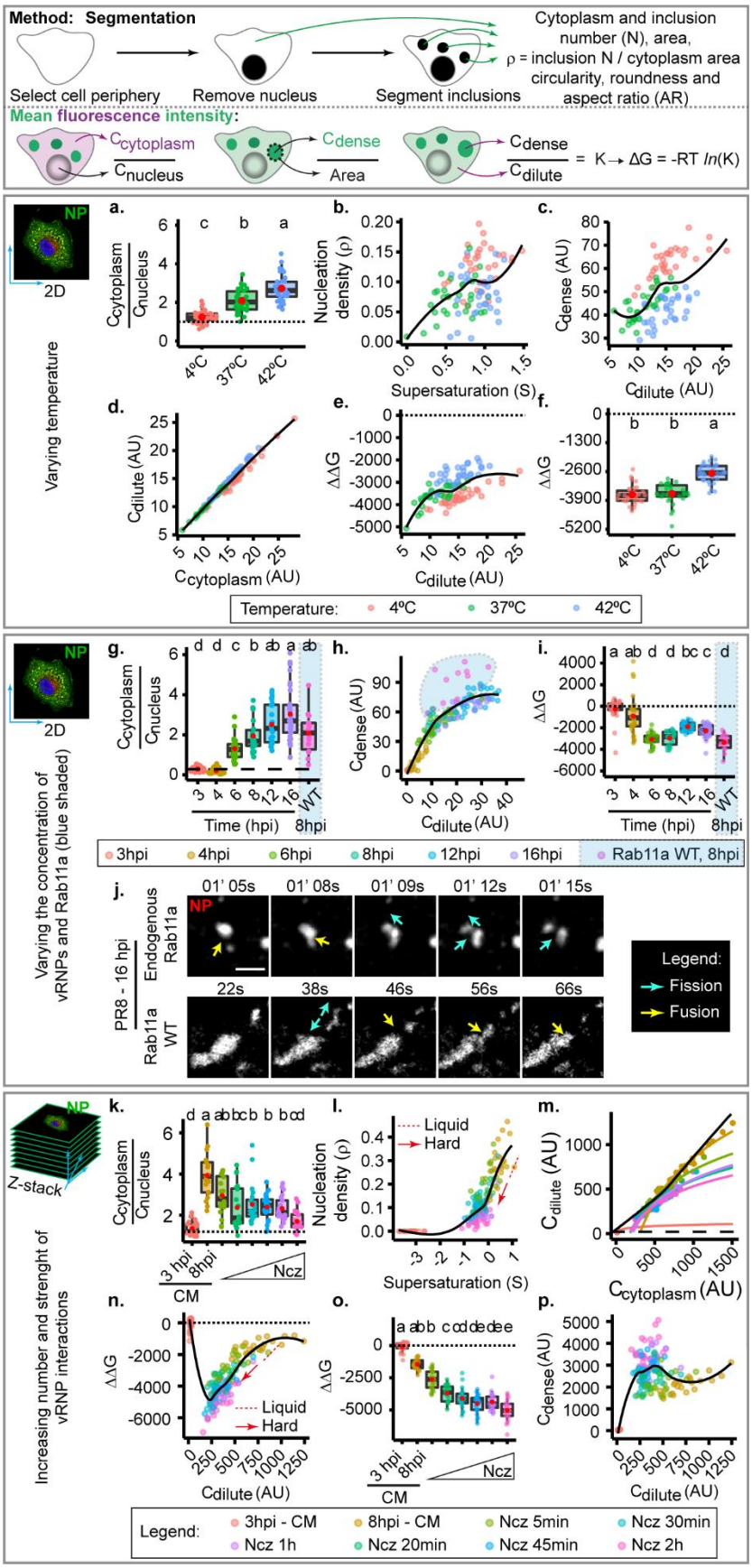
Method: Segmentation
Select cell periphery
Remove nucleus
Segment inclusions
Cytoplasm and inclusion number (N), area, ρ = inclusion N / cytoplasm area circularity, roundness and aspect ratio (AR)
Mean fluorescence intensity:
Ccytoplasm / Cnucleus
Cdense / Area
Cdense / Cdilute = K→ ΔG = -RT ln(K)
NP
2D
Varying temperature
Cytoplasm / Nucleus
Nucleation density (ρ)
Supersaturation (S)
Cdense (AU)
Cdilute (AU)
Cytoplasm (AU)
ΔΔG
4ºC
37ºC
42ºC
Temperature:
Varying the concentration of vRNPs and Rab11a (blue shaded)
Time (hpi)
8hpi
WT
3hpi
4hpi
6hpi
8hpi
12hpi
16hpi
Rab11a WT, 8hpi
PR8 - 16 hpi
Endogenous Rab11a
Rab11a WT
01' 05s
01' 08s
01' 09s
01' 12s
01' 15s
22s
38s
46s
56s
66s
Legend:
Fission
Fusion
Z-stack
Increasing number and strenght of vRNP interactions
3 hpi
8hpi
CM
Ncz
Liquid
Hard
Legend:
3hpi - CM
8hpi - CM
Ncz 5min
Ncz 30min
Ncz 1h
Ncz 20min
Ncz 45min
Ncz 2h

140

Fig. 1: The properties of IAV liquid inclusions are modified by modulating the number of interactions between vRNPs more than changing temperature or concentration of the components. Cells (A549 or GFP-Rab11a-WT) were infected at a multiplicity of infection (MOI) of 3 with PR8 and, at the indicated time points, were fixed and stained for NP by immunofluorescence (**a. - i.**, **k. - p.**). For live imaging (**j.**), cells (A549) were co-transfected with a plasmid encoding Rab11a-WT and mCherry-NP and simultaneously infected with PR8 virus at an MOI of 10 and were live imaged at 12hpi (n = –15 – 33). Above each boxplot, same letters indicate no significant difference between conditions, while different letters indicate a statistical significance at α = 0.05. Abbreviations: AU, arbitrary unit; WT, Rab11a Wild type; CM, complete; Ncz, nucleozin. **a.** Boxplot depicting the fold change in cytoplasmic to nuclear vRNP (NP, as proxy) concentration at different temperatures (ºC). *P* = 0.0362; one-way ANOVA followed by Tukey multiple comparisons of means. **b.** Scatter plot of nucleation density (ρ) versus degree of supersaturation (S), as a measure of propensity to remain dispersed in the cytoplasm, at different temperatures (ºC). **c.** Scatter plot of vRNP concentration within inclusions (C_{dense}, AU) versus surrounding cytoplasm (C_{dilute}, AU) at different temperatures (ºC). **d.** Scatter plot of C_{dilute} (AU) versus total cytoplasmic vRNP concentration $C_{cytoplasm}$ (AU) at different temperatures (ºC). **e.** Scatter plot of fold change in free energy of partition (ΔΔG), cal.mol^{-1}, at the indicated temperatures (ºC). **f.** Boxplot of fold change in free energy of partition (ΔΔG, cal.mol^{-1}) at different temperatures (ºC). *P* < 8.01e-16; one-way ANOVA followed by Tukey multiple comparisons of means. **g.** Boxplot depicting the fold change in the ratio of cytoplasmic to nuclear vRNPs concentration at different times of infection or when overexpressing Rab11a (WT) at 8hpi. *P* = 0; Kruskal Wallis Bonferroni treatment. **h.** Scatter plot of vRNP concentration within inclusions (C_{dense}, AU) versus surrounding cytosol (C_{dilute}, AU) at different times of infection (hpi) or Rab11a (WT) overexpression. **i.** Boxplot of fold change in free energy of partition (ΔΔG, cal.mol^{-1}) at different times of infection or with Rab11a (WT) overexpression at 8hpi. *P* = 0; Kruskal Wallis Bonferroni treatment. **j.** Time lapse images showing fission (blue arrow) and fusion (yellow arrow) events of inclusions (NP, as proxy) at 16hpi in cells expressing endogenous and overexpressed Rab11a (WT) (extracted from Supplementary Videos 1,2). Scale bar = 2 µm. **k.** Boxplot depicting the fold change in the ratio of cytoplasmic to nuclear vRNPs concentration before and after Ncz (5 mM) treatment at 8hpi. *P* = 6.16e-14; Kruskal Wallis Bonferroni treatment. **l.** Scatter plot of nucleation density (ρ, µm^{-2}) versus degree of supersaturation (S) changes before and after nucleozin (Ncz) treatment at 8hpi. **m.** Scatter plot of vRNP concentration outside inclusions (C_{dilute}, AU) versus total cytoplasmic concentration ($C_{cytoplasm}$, AU). Coloured lines are non-linear fitted models of grouped data points in the graph. **n.** Scatter plot of fold change in free energy of partition (ΔΔG, cal.mol^{-1}) versus surrounding cytoplasmic vRNP concentration (C_{dilute}, AU) before and after nucleozin (Ncz) treatment at 8hpi. **o.** Boxplot of fold change in free energy of partition (ΔΔG, cal.mol^{-1}) before and after nucleozin (Ncz) treatment at 8hpi. *P* = 0; Kruskal Wallis Bonferroni treatment. **p.** Scatter plot of vRNP concentration within inclusions (C_{dense}, AU) versus surrounding cytosol (C_{dilute}, AU) before and after nucleozin (Ncz) treatment at 8hpi. All the values calculated for the thermodynamics have been included as supplementary Table 1, distributed in different excel sheets for each parameter.

Nucleozin hardens IAV liquid inclusions in cultured cells and in *in vivo* conditions

Changing the strength of interactions impact viral inclusions the most. Therefore, we next sought to characterize if nucleozin altered their material properties. We first checked if nucleozin-treated viral inclusions maintained the ability to dissolve upon shock treatments. We observed that native inclusions responded to shock treatment as expected, however, nucleozin strongly held inclusions together that did not dissolve when exposed to either hypotonic or 1,6-hexanediol shock treatments (Fig. 2a, Extended Data Fig. 4a-c). This lack of response to shocks suggests that IAV inclusions undergo hardening when vRNP interactions are stronger.

To formally establish that IAV liquid inclusions can be hardened, we compared the dynamics of viral inclusions in the presence or absence of nucleozin using four different approaches. First, we assessed their movement and measured speed and displacement from their point of origin (Fig. 2b, Extended Data Fig. 4d,e). Native liquid-like inclusions (treated with sham vehicle - DMSO) display a highly stochastic movement and long displacement (0.838 ± 1.17 μm^2, median ± SD, n = 13, Supplementary Table 1), whilst nucleozin-hardened inclusions were less mobile with smaller displacement (0.057 ± 0.22 μm^2, median ± SD, n = 27, Supplementary Table 1) close to the point of origin (Fig. 2b, Extended Data Fig. 4d,e), even when analysed for long periods. In a second approach, we measured the time that two droplets take to relax to a sphere upon fusion by coarsening assays (shifting the aspect ratio from 2 to 1, Fig. 2c). DMSO-treated inclusions relax, shifting the aspect ratio from 2 to 1 fast, compared to nucleozin-treated inclusions which retain a stable aspect ratio over time (Fig. 2d,e), demonstrating stiffness. Moreover, DMSO-treated liquid inclusions are highly dynamic being able to fuse fast (5.8 ± 1.94; mean ± SEM, n = 10, Supplementary Table 1) while nucleozin-treated inclusions are less mobile and unable to fuse (n= 29, Supplementary Table 1) (Fig. 2f, Supplementary Table 1, Supplementary Videos 3,4). In a third approach, inclusion molecular dynamics was tested by Fluorescence Loss After Photoactivation (FLAPh). In a live imaging experiment, a region of interest (ROI) was photoactivated and its decay profile monitored for 120 seconds. DMSO- and nucleozin-treated inclusions exhibited distinct decay profiles, with half-life of 14.41 ± 0.9 sec (mean ± SEM) and 85.02 ± 19.8 sec, respectively (Fig. 2g-j, Extended Data Fig. 4f-h, Supplementary Table 1, Supplementary Video 5,6). This indicates that nucleozin treated inclusions become more static.

Lastly, we measured the internal rearrangement in viral inclusions. Because of the small size and highly dynamic nature of IAV inclusions, previous attempts to perform Fluorescence Recovery After Photobleaching (FRAP) experiments resulted in highly variable recovery rates that failed to explain the internal rearrangements undergoing in viral inclusions for two reasons: photobleaching the interior of the condensate was difficult, and there is a constant flow of material in and out of

IAV inclusions. As the microtubule depolymerising drug nocodazole largely blocks the movement of IAV inclusions, rendering them larger and more spherical [7], we opted for bleaching IAV inclusions upon treating them with nocodazole. In native conditions, we could observe internal rearrangement of vRNPs inside IAV inclusions, whilst in nucleozin-treated vRNP inclusions, the photobleached area remained unaltered, revealing stiffness (Fig. 2k, Supplementary Video 7,8). Taken together, DMSO and nucleozin treated IAV inclusions exhibit distinct response to shocks, dynamics, internal rearrangement and coalescing properties, supporting that nucleozin hardens IAV liquid inclusions.

Recently, the condensate-hardening drugs steroidal alkaloid cyclopamine and its chemical analogue A3 were shown to reduce viral titres in respiratory syncytial virus (RSV) infected mice [14]. However, at the organismal level, it was not demonstrated that RSV inclusion bodies in infected cells retained harded features. We challenged mice with X31 for 2 days. At 30 min, 1 h or 2 h before the collection of the lungs, each mouse was treated with PBS (sham vehicle) or 69 µg of nucleozin, administered intranasally (Fig. 2l) to analyse viral inclusions inside the cells of infected lung (Fig. 2l). Although, nucleozin was reported to affect viral titres by 1 log and increase survival of IAV (A/Vietnam/1194/04 H5N1) infected mice by 50% [27], the single use and the short duration of the treatment, did not result in differences in viral titres (Extended Data Fig. 5a). Under normal conditions, lung infected cells exhibited a punctate-like NP distribution. Upon nucleozin treatment, these cytosolic inclusion grew larger (PBS 2h: 0.101 ± 0.006 μm^2; Ncz 2h: 0.226 ± 0.012 μm^2, mean ± SEM, Supplementary Table 1) and were less abundant (inclusions per cell - PBS 2h: 226.2; Ncz 2h: 108.9, mean, Extended Data Fig. 5b,c, Supplementary Table 1;). This indicates that the pharmacological induced sticker activity of nucleozin retained the inclusion hardening phenotype *in vivo*[25,27] and serves as proof of concept that the material properties of condensates are suitable antiviral targets against influenza infection.

Given the possibility to harden IAV inclusions, it is important to define the molecular mechanisms conferring the material properties of these condensates, which remain elusive. As Rab11a drives the formation of IAV inclusions [3,7,10,11,19,22], we asked if nucleozin could artificially reform viral inclusion and mimic its behaviour in the absence of Rab11a (Fig. 2m). Stable cell lines expressing Rab11a dominant negative (DN) (henceforward Rab11a-DN) did not form IAV inclusions as expected maintaining vRNPs dispersed throughout the cytosol (Fig. 2n, Extended data Fig. 5 d). Interestingly, both Rab11a-WT and Rab11a-DN cell lines, in the presence of nucleozin, exhibited cytosolic puncta (despite smaller in Rab11a-DN lines, (Fig. 2n, Extended data Fig. 5 d,e). This

indicates that nucleozin bypasses the need for Rab11a to concentrate vRNPs. We next tested the fusion ability of nucleozin-induced IAV inclusions in Rab11a-DN lines. Unlike inclusions in WT cells, nucleozin-induced IAV inclusions in Rab11a-DN infected cells are not able to fuse in coarsening assays (Fig. 2 n,o, Supplementary Video 9,10), are irregularly shaped (Extended Data Fig. 5d,e), more stable (with lower Gibbs free energy, Fig. 2p) and more deficient in producing progeny virions (Extended data Fig. 5f). In sum, the liquid properties of IAV inclusions derived from flexible intersegment interactions amongst vRNP that upon stabilization harden to form stiff aggregates.

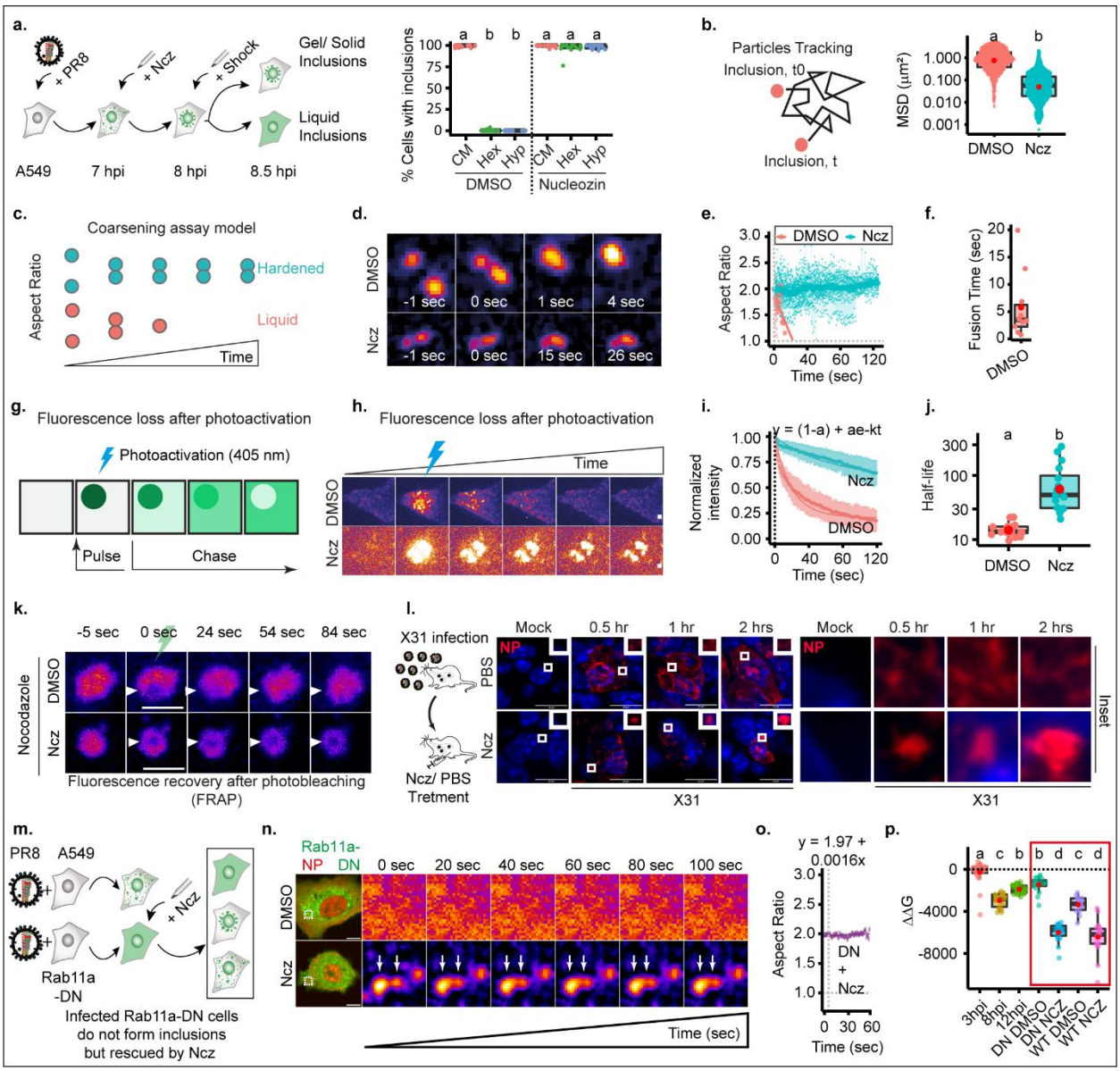

Fig. 2: IAV inclusions' hardening changes its material properties. **a.** Experimental schematics and data to assess if Ncz treated IAV inclusions dissolve in response to shocks. A549 cells were infected at an MOI of 3 with PR8 virus and treated with Ncz or DMSO at 7hpi. An hour later, cells were treated for 30 min with 80% water (hypotonic shock, Hyp), with 1,6-hexanediol (Hex) or complete media (CM) as control. Cells were fixed at 8.5h, stained for NP by immunofluorescence and the percentage of cells with IAV inclusions was scored manually. $P = 0$; Kruskal Wallis Bonferroni treatment. **b. – j.** A549 cells were transfected with plasmids encoding either GFP-NP (**b. - f.**, **i. – j.**) or photoactivatable GFP-NP (**g. – h.**) and simultaneously infected with PR8 virus at an MOI of 10, being live imaged from 12hpi onwards. **b.** Scheme showing how IAV inclusions were tracked over time and plot depicting the resulting mean square displacement (μm^2) of IAV inclusions in the presence or absence of Ncz. $P = 0$; Kruskal Wallis Bonferroni treatment. **c.** Schematics of the coarsening assay model, in which liquid and hardened IAV inclusions are represented by orange and blue dots, respectively. Unlike hardened inclusions, native liquid inclusions to fuse and relax to a spherical droplet. **d.** Pseudo-colored time-lapse images of coalescing viral inclusions (GFP-NP used as proxy; extracted from Supplementary Videos 3,4) in the presence or absence of Ncz. **e.** Aspect ratio (AR) was used as a measure of IAV inclusion coalescence into a sphere. Mean AR per time was fitted to a linear model (bold coloured lines). Horizontal grey dash lines depict a perfect sphere (aspect ratio = 1). **f.** Boxplot of the fusion time (sec) of IAV liquid inclusions. Dots represent fusion time of individual fusion event. **g.** Schematic of a fluorescence loss after photoactivation (FLAPh) experiment. **h.** Time lapse pseudo-colour images showing the fluorescence loss in photoactivated IAV inclusions (photoactivatable GFP-NP used as proxy) upon treatment with nucleozin or DMSO (extracted from Supplementary Videos 5,6). **i.** Fluorescence intensity decay of photoactivated (PhotoGFP-NP) normalised to the corresponding IAV inclusions expressing cherryNP. Coloured lines are single exponential model fitting ($y_0 = (1-a) + ae^{-kt}$) of the data point, dots are the mean of the data per second, and vertical lines denote the standard deviation (SD) per time (sec). **j.** Half-life ($t_{1/2} = \frac{In(2)}{k}$) of liquid and hardened IAV inclusions decay post-activation (sec). $P = 1.386e-6$; Kruskal Wallis Bonferroni treatment. **k.** A549 cells were transfected with plasmids encoding mcherry-NP and co-infected with PR8 virus at an MOI of 10. At 12hpi, cells were treated with nocodazole (10 μg/mL) for 2h to reduce the highly stochastic motion of liquid IAV inclusions and subsequently treated with DMSO or Ncz. Small regions inside IAV inclusions were photobleached to assess internal rearrangement of vRNPs (mCherry-NP as proxy). Time lapse pseudocolor images shows the fluorescence recovery after photobleaching (FRAP, extracted from Supplementary Videos 7,8). Bar = 2 μm **l.** Mice were intranasally infected with 4000 plaque forming units (PFU) of X31 virus, and after 2 days were treated with PBS or 69 μg of nucleozin at 30 min, 1h or 2h before the collection of the lungs. Immunofluorescence images show sections of lung tissue stained for NP (red) and nucleus (blue) after PBS or Ncz treatment. **m.-p.** A549 cells stably expressing a dominant negative version of Rab11a fused to GFP (Rab11a-DN) were transfected with cherry-NP (**n., o.)** or later stained for NP **(p.)** and infected (PR8, MOI=3) before treating with Ncz or DMSO at 12hpi. **m.** Schematic depicting the possible outcomes when Rab11a-DN cell lines are treated with Ncz **n.** Time lapse pseudocolor images show fusion of IAV inclusions in a coarsening assay of PR8

infected Rab11a-DN cell line treated with Ncz or DMSO (extracted from Supplementary Videos 9,10). **o.** Plot depicting the aspect ratio of fusing inclusions over time in infected Rab11a-DN cell line treated with Ncz. **p.** Boxplot comparing the fold change in free energy of partition (ΔΔG, cal.mol^{-1}) of IAV inclusions, normalized to 3hpi, in PR8 infected cells overexpressing Rab11a (DN and WT, red box) at 12 hpi. $P < 0.01$; Kruskal Wallis Bonferroni treatment. Cells were treated with DMSO or nucleozin and values compared to those obtained in control cells expressing endogenous Rab11a (at 8 and 12 hpi). Above each boxplot, same letters indicate no significant difference between them, while different letters indicate a statistical significance at $\alpha = 0.05$.

IAV infection alters the solubility profile in cells

Next, to understand how both the viral and host cellular proteomes remodel because of IAV infection in the absence and presence of nucleozin, we used a recently developed quantitative mass spectrometry-based approach called solubility proteome profiling (SPP) [28]. This is a lysate centrifugation assay which can distinguish the soluble (supernatant) from insoluble (dense assemblies) protein pools. The majority of proteins annotated to be part of membraneless organelles, as well as many cytoskeletal proteins, exhibit prominent insolubility. In SPP, two aliquots of cellular lysates are extracted with either a strong (SDS) or a mild (NP40) detergent. Protein extracted with SDS represent the total proteome, while the supernatant of NP40-extracted lysate represents the soluble sub-pool. The ratio of NP40- and SDS-derived protein abundance represents the solubility of a protein. Protein solubility is proxy to track phase transition events in different cellular states. However, this measurement cannot distinguish between different events, such as solidification, phase separation, percolation and gelation [2] that may underlie the phase transition.

To establish the physiological changes in protein abundance and solubility occurring along the infection, we performed a time course of PR8 infection in A549 cells followed by SPP as shown in Fig. 3a. Overall we identified and quantified 6,619 host proteins and 10 viral proteins with at least 2 unique peptides. In comparison to the uninfected cells, 174 host proteins underwent changes in abundance along the infection time course (Supplementary Table 2,3, Extended Data Fig. 6). Euclidean distances-based clustering of the abundance profiles of these proteins resulted in 6 distinct clusters which enriched for proteins associated with different GO terms “Biological processes” and/or “Cellular Compartments” (Supplementary Table 4). A majority of these proteins (78.2 %, 136 proteins) exhibited a consistent decrease in abundance in line with the previous observations [29], while a small subset (21.8%, 38 proteins) exhibited a sharp increase in abundance in response to the infection. The downregulated host proteins (from cluster 1-3) are

associated with processes such as extracellular matrix organization, cell cycle and cell adhesion. The upregulated proteins (from cluster 6) were primarily effectors of type-I interferon pathway (Extended Data Fig. 6), in agreement with the well-known anti-viral response to the infection mounted by host cell.

In terms of protein solubility, we observe no significant changes in the host proteome until 4 hpi (Fig. 3b-e). However, from 8hpi, several host proteins underwent changes in solubility (236 and 171, loosing and gaining solubility, respectively) providing cues on how infection remodels the cellular systems (Fig. 3b-e). Euclidean distance-based clustering of the solubility profiles of host proteins (significantly changing) along the time course resulted in 6 distinct clusters (Fig. 3b-e). We found that proteins involved in interferon pathway, cell division, cellular RNA biology, and ER processes lost solubility, whilst metabolic related processes, mitochondrial organization and ribosomal RNA processing became more soluble (Fig. 3d). The phase transitions in the cytosol correlated with inner mitochondrial membrane, cytoskeleton, translation, and cell-substrate junction proteins (Fig. 3e). Interestingly, changes progressed steadily until 12 hpi. More so, between 12 and 16 hpi, the profile altered in many ways; for instance, cluster 1, 4 and 6 plateaus, cluster 2 and 5 aggravate the slope and cluster 3 reverts trend, which may be related with cytopathic effects (Fig. 3b-d). It is noteworthy that only 35 host proteins (among 407 proteins that alter solubility) – overrepresented in interferon pathway related proteins – change in both abundance and solubility. This indicates that except for interferon related proteins, changes in protein concentration were not the underlying cause of the changes in solubility (Supplementary Table 2-3, Extended Data Fig. 6f).

We observed a time dependent increase in abundance for all identified and quantified viral proteins (Extended Data Fig. 6e), as expected, from uninfected to infected state. In terms of solubility, we found 5 viral proteins, namely all vRNP components PB1, PB2, PA and NP (P <0.0001 at least), and the non-structural protein-1 (NS1, P < 1,31E-08 at least, Fig. 3f), became strongly insoluble with infection from 8 hpi. At a later stage of infection (beyond 12 hpi), neuraminidase (NA) became modestly insoluble (fold changes of 0.64, P = 0.008639, and 0.47, P = 0.000334, at 12 and 16hpi, respectively, Fig. 3f and Supplementary Table 3). NS1 and NA undergoing phase transitions has not been reported. Hence, to validate our system-level observation on the viral protein NS1, we used fluorescence microscopy to track its subcellular location along with a key host protein – a E3 ubiquitin ligase Tripartite motif 25 (TRIM25) [30,31]. TRIM25 activates an antiviral state once an infected cell senses pathogen-associated molecular

patterns. NS1 counteracts this activation by directly binding to TRIM25 [32]. TRIM25 also exhibited significant insolubility at 12 and 16 hpi (fold changes = 0.34, 0.31, *P* = 5,12E-04 and 0,000306289 respectively, Supplementary Table 2-3) in our solubility assay. This protein was recently shown to undergo a type of phase transition, de-mixing from the cytosol by liquid-liquid phase separation [33]. We observe a strong co-localization signal for NS1 and TRIM25 from 12 hpi that accumulated in non-spherical, punctate-like structures in the cytosol [33] (Fig. 3g) by immunofluorescence, corroborating our finding from MS-based assay.

Overall, our results indicate that many host proteins undergo dynamic phase transitions during IAV infection. Of note, only 40 proteins (6.7%), including 10 viral proteins, changed abundance and solubility at the same time, out of 597 proteins suffering alterations, which means that alterations in concentration were not the underlying cause of the changes in solubility (Extended Data Fig. 6d,f). Among the viral components, vRNPs which are synthesized in the nucleus and transported to the cytosol where they accumulate in viral inclusions exhibit high insolubility.

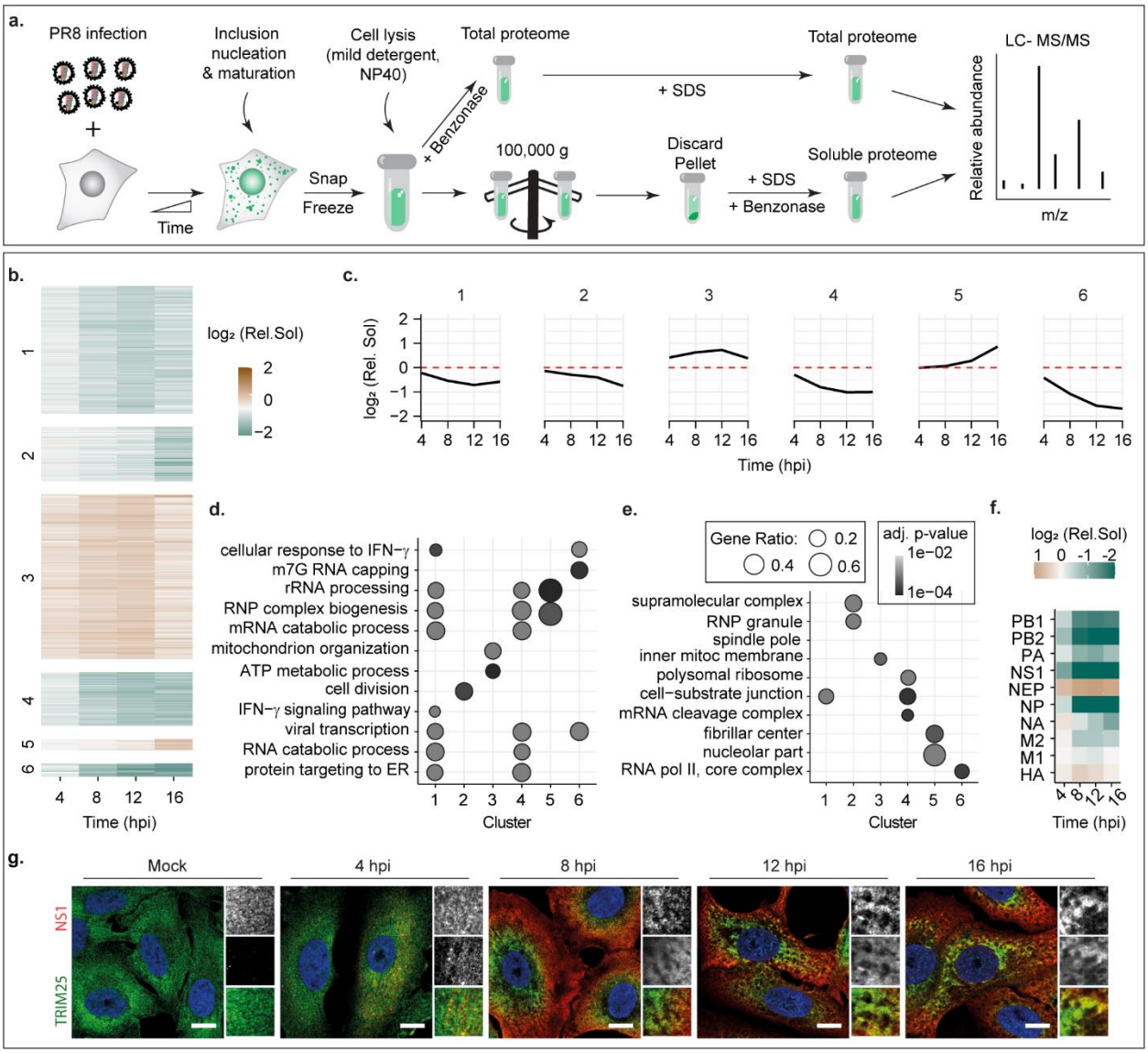

Fig. 3: Host and viral factors change solubility in a proteome-wide manner. A549 cells were mock-infected for 12 hours or PR8 infected for 4, 8, 12 & 16 hours at a multiplicity of infection (MOI) of 5. **(a - f.)** Thereafter, cells were lysed in mild (NP40) or strong detergent (SDS), and NP40 lysate was ultracentrifuged (100,000 g) to pellet materials in condensates from the soluble fraction in the supernatant. Soluble and total host and viral proteome were identified by LC-MS/MS and solubility was determined as the ratio of soluble NP40- to SDS- derived total proteome abundances at the indicated hour post infection (hpi). **a.** Schematic of solubility proteome profiling (SPP) (see methods for detailed description). **b.** Hierarchically clustered heat map showing relative solubility of host proteome at the indicated times of infection in comparison to 12 h of mock-infection. Significant solubility changes were grouped in 6 distinct clusters based on the Euclidean distances. **c.** Line plot representing the median relative solubility of host proteins from the 6 distinct clusters (from **b.**, in $\log_2$ scale) in relation to the time of infection. Red dashed line indicates no change in relative

solubility (log_2 (Rel. Sol) = 0). log_2 (Rel. Sol) > 0 means more soluble than control (12 hr Mock) and vice-versa. **d.** Dot plots representing the gene ontology (GO), biological processes over-represented among significant hits from proteome-wide solubility (shown in panel **b.**). Selected enriched biological processes in relation to the individual clusters (1-6) are shown. The size of the dots relates with the ratio of genes per cluster that belong to the indicated biological process, and the grey fill shows the adjusted p-value. **e.** Dot plots representing the gene ontology (GO), cellular compartments over-represented among significant hits from proteome-wide solubility (shown in panel b). Selected enriched cellular compartments for the individual clusters (1-6) are shown. The size of dot relates with the ratio of genes per cluster that belong to the indicated cellular compartment, and the grey fill shows the adjusted p-value. **f.** Heat map depicting the relative solubility (log_2) of viral proteins at the indicated times of infection in comparison to 12hrs mock infection. **g.** Localisation of host protein TRIM25 (in green, and upper inlet) and viral protein NS1 (in red, middle inlet) by immunofluorescence. Inlets show areas of colocalization between TRIM25 and NS1. Nuclei stained using Hoechst (blue). Scale bar = 10 µm.

Nucleozin induced insolubility on vRNPs relates to formation of IAV liquid inclusions.

To identify if the insolubility of vRNPs relates to liquid inclusion formation, we compared proteome abundance and solubility profiles of Rab11a-DN cell lines – where the formation of liquid inclusion is blocked (Fig. 2m,n, Extended Data Fig. 5d) – with that of Rab11a-WT cell lines at 12 hpi (Fig. 4a,b). Rab11a-DN cells exhibited changes in abundance of 582 proteins relative to Rab11a-WT cells (Supplementary Table 5, Extended Data Fig. 7a) and these proteins related to DNA damage, phosphatase activity, cell adhesion, nucleolar RNA processing, cell cycle and cholesterol metabolism (Extended Data Fig. 7c). Rab11a-DN cells exhibited altered solubility for 127 host proteins (Supplementary Table 6, Fig. 4b) in comparison to the Rab11a-WT cells. Proteins that exhibited increased solubility in Rab11a-DN line were over-represented in cellular processes such as RNA biology, ribosome processing, ribonucleoprotein complex biology (see Extended Data Fig. 7d and Supplementary Table 6 for overlapping proteins). Interestingly, proteins associated with mitochondrial translation exhibited decreased solubility in Rab11a-DN lines (Fig. 4b, Extended Data Fig. 7d). We sought to validate our findings and understand the association between mitochondria and IAV inclusions. This association could be direct or indirect, hence, we started by establishing whether mitochondria interacted with viral inclusions selectively using immunofluorescence imaging to visualize their local interactions. We found that mitochondria localised to the cell periphery in a significant manner after 8 hpi. ($p < 0.000001$), and that at this time point, many mitochondria associated with cytosolic IAV inclusions (Fig. 4c,d) [3]. The reason for mitochondrial-inclusion association is currently being investigated.

Next, we sought to understand the system-wide response triggered by nucleozin. To achieve this, we measured the protein solubility and abundance changes of both host and viral proteomes in response to 1 h treatment with nucleozin in Rab11a-WT and Rab11a-DN cells infected with PR8 for 12 h (Fig 4a,e-h, Supplementary Table 7,8). Nucleozin-treatment did not induce significant alteration in host proteome abundance in both cell lines (Fig. 4e). Similarly, no major changes in terms of protein solubility were observed for the host proteome during this treatment period (Fig. 4f). Overall, our results suggest that nucleozin does not induce changes in cellular protein levels or their solubility.

In terms of the viral proteome, the abundance of all protein components of vRNPs (NP, PB1, PB2, PA and M1) show a modest increase in Rab11a-DN cell lines (Extended Data Fig. 7b). On the solubility level, NP exhibited a prominent change. NP remains more soluble in Rab11a-DN lines compared to Rab11a-WT infected cells (Fig. 4h,i). This corroborates with the observation that vRNPs remain uniformly distributed in Rab11a-DN cells (Fig. 2 m-p, Extended Data Fig. 5d). Upon nucleozin treatment, SPP data reveals that the solubility of NP remains unaltered in Rab11a-WT cells, while increasing the proportion of NP in insoluble pool in Rab11a-DN cells (Fig 4h). Although, SPP data was similar, we observed IAV inclusions growing larger and hardening upon nucleozin treatment on the microscopy level in Rab11a-WT cells (Extended Data Fig. 5d). This can be explained as vRNPs are already insoluble in viral inclusions before nucleozin treatment and the net increase in size of the inclusions does not result in higher insolubility of vRNPs. Both SPP and microscopy complement each other in the case of Rab11a-DN cells as viral inclusions change from soluble to insoluble and become bigger upon nucleozin treatment. Overall, the data substantiates our finding that vRNPs form Rab11a-dependent insoluble and liquid inclusions which undergo a distinctive phase transition upon nucleozin treatment.

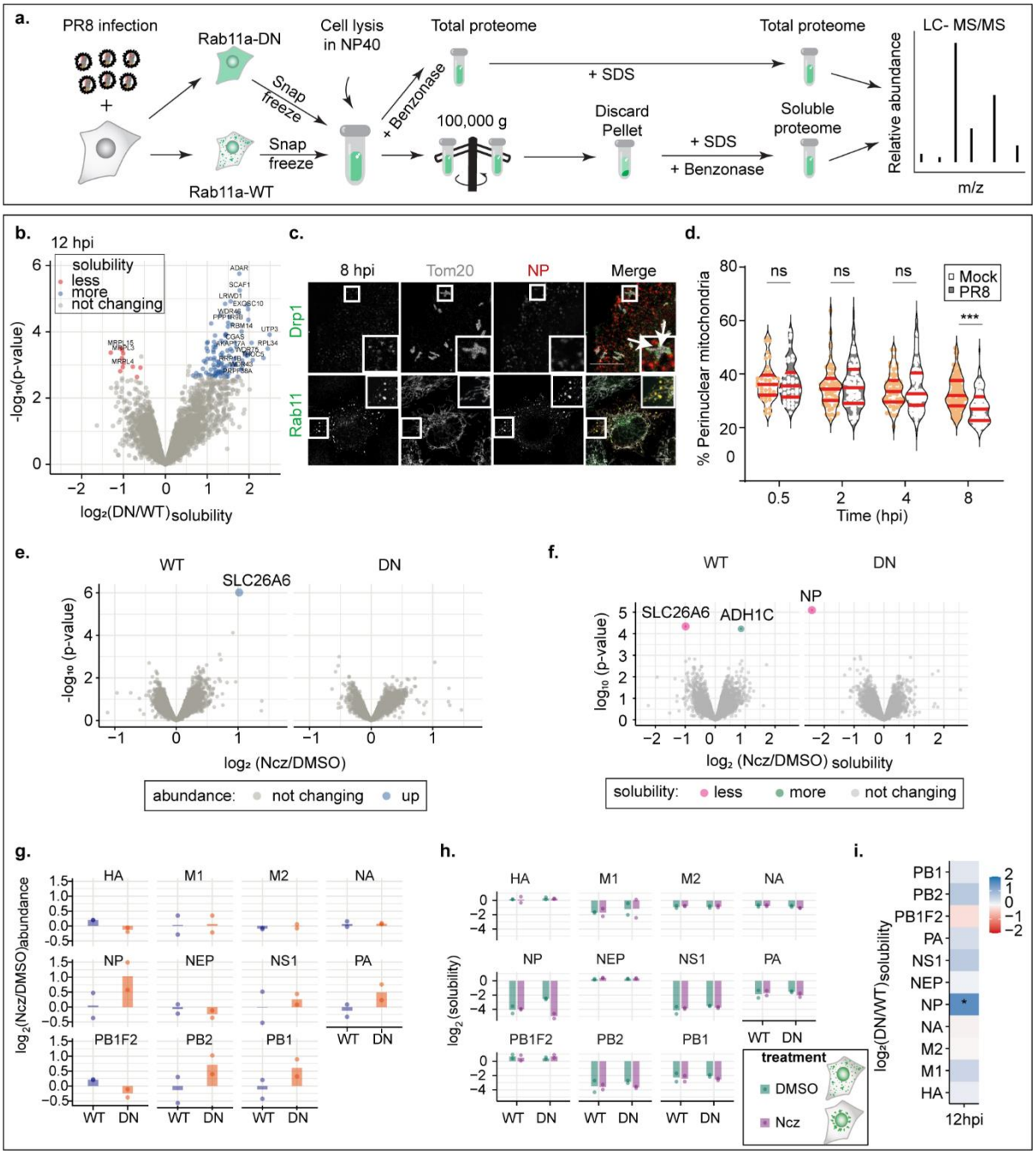

Fig. 4: Inclusion (in)solubility is Rab11a-dependent and interacts with mitochondria. (**a. – b., e. – h.**) Cell lines constitutively expressing GFP-Rab11a-WT and GFP-Rab11a-DN were infected for 12 h with PR8 at a multiplicity of infection (MOI) of 5 and treated with nucleozin (Ncz) or sham vehicle (DMSO) (**e. - h.**). Thereafter, cells were lysed in mild (NP40) or strong detergent (SDS), while NP40 lysate was ultracentrifuged (100,000 g) to pellet materials in condensates from the soluble fraction in the supernatant. Soluble and total host and viral proteome were identified by LC-MS/MS and solubility was determined as the ratio of soluble NP40- to SDS- derived total proteome abundances at the indicated hour post infection (hpi). **a.** Schematic of experimental workflow for solubility proteome profiling (SPP) of infected GFP-

(Rab11a-WT and Rab11a-DN) cell lines (*see methods*). **b.** Volcano plot of host proteome solubility in a 12-hr infected Rab11a-DN cell line relative to Rab11a-WT line. Red and blue dots signify insoluble (mitochondria) and soluble proteins respectively. **c.** Immunofluorescence images showing vRNPs associate with mitochondria. At 8hpi, HeLa cells infected with PR8 at an MOI of 3 were fixed and stained for vRNPs (using NP as proxy, red), mitochondria (Tom20, grey) and Drp1 or Rab11 (green). Insets show areas of vRNP/ mitochondria/Drp1 and vRNP/ mitochondria/Rab11a aggregation. Note that Drp1 may serve as a bridge between mitochondria and vRNPs. **d.** Violin plot of single cell analysis of mitochondria distributions during infection (*see methods*). ns, not significant; $P < 0.0001$; Kruskal Wallis Bonferroni treatment. **e.** Volcano plot representing relative host protein abundance in Rab11a-WT and Rab11a-DN infected cell lines (at 12 hpi) after treatment with nucleozin or DMSO. Differentially upregulated proteins in these conditions (statistical significance – *see methods*) are indicated in blue dots. **f.** Volcano plot representing relative solubility of host and viral proteins in Rab11a-WT and Rab11a-DN infected cell lines (at 12 hpi) after treatment with nucleozin. Differentially soluble proteins in these conditions (statistical significance – *see methods*) are indicated in pink and green dots. **g.** Bar graph comparing viral proteins abundances (in $\log_2$ scale) in Rab11a-WT and Rab11a-DN cell lines PR8-infected (12 hpi) and treated with either nucleozin or DMSO. **h.** Bar graph comparing solubility (in $\log_2$ scale) of viral proteins when PR8 infected (12 hpi) Rab11a-WT and Rab11a-DN cell lines were treated with either nucleozin (Ncz) or sham vehicle (DMSO). . **i.** Heat map showing the $\log_2$ relative solubility of all influenza proteins (y-axis) in Rab11a-DN mutant cell line in comparison to wild type Rab11a-WT cells at 12 hours post infection (hpi). Asterisk (*) represents proteins changing in a statistically significant manner (*see methods*).

DISCUSSION

Targeting the material properties of biological condensates holds great therapeutic potential for many diseases including neurodegeneration and cancer, and we have shown its applicability for viral infections. Understanding how the material properties of cellular condensates impact the viral lifecycle or host response to infection is an emerging field [34]. Distinct cellular states (such as starvation, stress, etc) and viral infections (such as rabies, vesicular stomatitis virus, hRSV, measles, etc) give rise to condensates reported to form by phase transitions such as liquid-liquid phase separation, phase-separated assisted percolation, reentrant phase transition, etc [35]. Demixing from the surrounding media implies a thermodynamic preference of alike molecules to interact and self-sort in ways that are well understood for binary systems but deviate considerably for muticomponent systems, even *in vitro* [16,36,37]. In living, multicomponent systems that operate at non-equilibrium, small alterations in the interactions, caused by changes in the environment or the interactome of the condensate, originate different self-assembled structures [16]. For example, concentration increase is not uniquely associated with more ordered structures, as higher ordered

structures were reported to arise in response to dilution [38]. Therefore, understanding how the physical modulators of phase transitions (such as temperature, concentration, strength of interactions, pH, ionic strength, and salt concentration) impact the properties of condensates is essential in designing condensate-targeting drugs or material science of lipid nanoparticles [39]. We speculate that during IAV infection, phase transition originates a demixed population of vRNPs within viral inclusions where vRNPs engage in multiple and distinct intersegment interactions bridging cognate vRNP-Rab11 units on flexible membranes [9,40-44]. How demixing could promote formation of complete genomes and how these would be excluded from viral inclusions to reach the plasma membrane remains unknown. Our study shows that inclusions may be hardened by targeting vRNP interactions. Such targeting may prevent off-target effects, especially by developing compounds able to distinguish free vRNP components from those in the supramolecular complex, however the cost is evolving escape mutants. Therefore, a concern to address is how to design suitable combinatory therapies able to reduce their emergence. Since single nucleotide mutations underpin numerous resistance mechanisms to antivirals [45], an alternative is to engineer condensate hardening drugs that require multiple amino acid changes for escaping the compound imposed blockade. Another strategy could be drug targeting of broad-spectrum pro-viral host factors. Recently, Rab11a has emerged as a key factor for the replication of members of many unrelated viral families relevant for human health (*Bunyaviridae*, *Filoviridae*, *Orthomyxoviridae*, *Paramyxoviridae* and *Pneumoviridae*) [7,46-49]. Targeting this protein may work as a pan-antiviral. From our work, we know that overstimulation of Rab11a concentrates more vRNP in liquid inclusions, but mildly alters their material properties, despite Ostwald ripening and Brownian motion coalescence. Accumulating independent evidence shows that blocking Rab11 pathway, directly or indirectly, hampers viral infection. Hence, future research could continue exploring this alternative.

Additionally, our finding that IAV infection induces extensive changes in the solubility of many host and viral proteins raises the hypothesis that this may be the case for other viruses. Current studies are finding that phase transitions (of many different types) serve to control distinct cellular processes during viral infection including metabolism, antiviral responses as well as viral replication [50]. How immunometabolism is linked to phase transitions is currently not known [51]. Our results open many new avenues on how viruses modify or regulate cellular function via condensates and support the development of condensate hardening therapies to combat diseases.

REFERENCES

1 Etibor, T. A., Yamauchi, Y. & Amorim, M. J. Liquid Biomolecular Condensates and Viral Lifecycles: Review and Perspectives. *Viruses* **13**, doi:10.3390/v13030366 (2021).

2 Alberti, S. & Hyman, A. A. Biomolecular condensates at the nexus of cellular stress, protein aggregation disease and ageing. *Nat Rev Mol Cell Biol* **22**, 196-213, doi:10.1038/s41580-020-00326-6 (2021).

3 Alenquer, M. *et al.* Influenza A virus ribonucleoproteins form liquid organelles at endoplasmic reticulum exit sites. *Nature Communications* **10**, 1629, doi:10.1038/s41467-019-09549-4 (2019).

4 Pons, M. W. A reexamination of influenza single-and double-stranded RNAs by gel electrophoresis. *Virology* **69**, 789-792, doi:10.1016/0042-6822(76)90508-0 (1976).

5 Amorim, M. J. A Comprehensive Review on the Interaction Between the Host GTPase Rab11 and Influenza A Virus. *Frontiers in Cell and Developmental Biology* **6**, doi:10.3389/fcell.2018.00176 (2019).

6 Hutchinson, E. C., von Kirchbach, J. C., Gog, J. R. & Digard, P. Genome packaging in influenza A virus. *J Gen Virol* **91**, 313-328, doi:10.1099/vir.0.017608-0 (2010).

7 Amorim, M. J. *et al.* A Rab11- and microtubule-dependent mechanism for cytoplasmic transport of influenza A virus viral RNA. *J Virol* **85**, 4143-4156, doi:10.1128/JVI.02606-10 (2011).

8 Avilov, S. V., Moisy, D., Naffakh, N. & Cusack, S. Influenza A virus progeny vRNP trafficking in live infected cells studied with the virus-encoded fluorescently tagged PB2 protein. *Vaccine* **30**, 7411-7417, doi:10.1016/j.vaccine.2012.09.077 (2012).

9 Chou, Y. Y. *et al.* Colocalization of different influenza viral RNA segments in the cytoplasm before viral budding as shown by single-molecule sensitivity FISH analysis. *PLoS Pathog* **9**, e1003358, doi:10.1371/journal.ppat.1003358 (2013).

10 Eisfeld, A. J., Kawakami, E., Watanabe, T., Neumann, G. & Kawaoka, Y. RAB11A is essential for transport of the influenza virus genome to the plasma membrane. *J Virol* **85**, 6117-6126, doi:10.1128/JVI.00378-11 (2011).

11 Lakdawala, S. S. *et al.* Influenza a virus assembly intermediates fuse in the cytoplasm. *PLoS Pathog* **10**, e1003971, doi:10.1371/journal.ppat.1003971 (2014).

12 Momose, F. *et al.* Apical transport of influenza A virus ribonucleoprotein requires Rab11-positive recycling endosome. *PLoS One* **6**, e21123, doi:10.1371/journal.pone.0021123 (2011).

13 Lopez, N. *et al.* Deconstructing virus condensation. *PLoS Pathog* **17**, e1009926, doi:10.1371/journal.ppat.1009926 (2021).

14 Risso-Ballester, J. *et al.* A condensate-hardening drug blocks RSV replication in vivo. *Nature* **595**, 596-599, doi:10.1038/s41586-021-03703-z (2021).

15 Klein, I. A. *et al.* Partitioning of cancer therapeutics in nuclear condensates. *Science* **368**, 1386-1392, doi:10.1126/science.aaz4427 (2020).

16 Riback, J. A. *et al.* Composition-dependent thermodynamics of intracellular phase separation. *Nature* **581**, 209-214, doi:10.1038/s41586-020-2256-2 (2020).

17 Sanders, D. W. *et al.* Competing Protein-RNA Interaction Networks Control Multiphase Intracellular Organization. *Cell* **181**, 306-324 e328, doi:10.1016/j.cell.2020.03.050 (2020).

18 Shimobayashi, S. F., Ronceray, P., Sanders, D. W., Haataja, M. P. & Brangwynne, C. P. Nucleation landscape of biomolecular condensates. *Nature* **599**, 503-506, doi:10.1038/s41586-021-03905-5 (2021).

19 Vale-Costa, S. *et al.* Influenza A virus ribonucleoproteins modulate host recycling by competing with Rab11 effectors. *J Cell Sci* **129**, 1697-1710, doi:10.1242/jcs.188409 (2016).

20 Weber, S. C. & Brangwynne, C. P. Inverse size scaling of the nucleolus by a concentration-dependent phase transition. *Curr Biol* **25**, 641-646, doi:10.1016/j.cub.2015.01.012 (2015).
21 Hernandez-Vega, A. *et al.* Local Nucleation of Microtubule Bundles through Tubulin Concentration into a Condensed Tau Phase. *Cell Rep* **20**, 2304-2312, doi:10.1016/j.celrep.2017.08.042 (2017).
22 Veler, H. *et al.* The C-terminal domains of the PB2 subunit of the influenza A virus RNA polymerase directly interact with cellular GTPase Rab11a. *J Virol*, jvi0197921, doi:10.1128/jvi.01979-21 (2022).
23 Kawakami, E. *et al.* Strand-specific real-time RT-PCR for distinguishing influenza vRNA, cRNA, and mRNA. *J Virol Methods* **173**, 1-6, doi:10.1016/j.jviromet.2010.12.014 (2011).
24 Nakamura, H. *et al.* Intracellular production of hydrogels and synthetic RNA granules by multivalent molecular interactions. *Nat Mater* **17**, 79-89, doi:10.1038/nmat5006 (2018).
25 Amorim, M. J., Kao, R. Y. & Digard, P. Nucleozin targets cytoplasmic trafficking of viral ribonucleoprotein-Rab11 complexes in influenza A virus infection. *J Virol* **87**, 4694-4703, doi:10.1128/JVI.03123-12 (2013).
26 Nakano, M. *et al.* Ultrastructure of influenza virus ribonucleoprotein complexes during viral RNA synthesis. *Commun Biol* **4**, 858, doi:10.1038/s42003-021-02388-4 (2021).
27 Kao, R. Y. *et al.* Identification of influenza A nucleoprotein as an antiviral target. *Nat Biotechnol* **28**, 600-605, doi:10.1038/nbt.1638 (2010).
28 Sridharan, S. *et al.* Proteome-wide solubility and thermal stability profiling reveals distinct regulatory roles for ATP. *Nat Commun* **10**, 1155, doi:10.1038/s41467-019-09107-y (2019).
29 Nacken, W., Schreiber, A., Masemann, D. & Ludwig, S. The Effector Domain of the Influenza A Virus Nonstructural Protein NS1 Triggers Host Shutoff by Mediating Inhibition and Global Deregulation of Host Transcription When Associated with Specific Structures in the Nucleus. *mBio* **12**, e0219621, doi:10.1128/mBio.02196-21 (2021).
30 Koliopoulos, M. G. *et al.* Molecular mechanism of influenza A NS1-mediated TRIM25 recognition and inhibition. *Nat Commun* **9**, 1820, doi:10.1038/s41467-018-04214-8 (2018).
31 Watanabe, T., Imai, M. & Kawaoka, Y. NS1 is the fluid for "flu-transmission". *Proc Natl Acad Sci U S A* **114**, 11012-11014, doi:10.1073/pnas.1715239114 (2017).
32 Gack, M. U. *et al.* Influenza A virus NS1 targets the ubiquitin ligase TRIM25 to evade recognition by the host viral RNA sensor RIG-I. *Cell Host Microbe* **5**, 439-449, doi:10.1016/j.chom.2009.04.006 (2009).
33 Yang, P. *et al.* G3BP1 Is a Tunable Switch that Triggers Phase Separation to Assemble Stress Granules. *Cell* **181**, 325-345 e328, doi:10.1016/j.cell.2020.03.046 (2020).
34 Meganck, R. M. & Baric, R. S. Developing therapeutic approaches for twenty-first-century emerging infectious viral diseases. *Nat Med* **27**, 401-410, doi:10.1038/s41591-021-01282-0 (2021).
35 Milin, A. N. & Deniz, A. A. Reentrant Phase Transitions and Non-Equilibrium Dynamics in Membraneless Organelles. *Biochemistry* **57**, 2470-2477, doi:10.1021/acs.biochem.8b00001 (2018).
36 Klosin, A. *et al.* Phase separation provides a mechanism to reduce noise in cells. *Science* **367**, 464-468, doi:10.1126/science.aav6691 (2020).
37 Snead, W. T. *et al.* Membrane surfaces regulate assembly of ribonucleoprotein condensates. *Nat Cell Biol*, doi:10.1038/s41556-022-00882-3 (2022).
38 Helmich, F. *et al.* Dilution-induced self-assembly of porphyrin aggregates: a consequence of coupled equilibria. *Angew Chem Int Ed Engl* **49**, 3939-3942, doi:10.1002/anie.201000162 (2010).
39 Hermans, T. M. *et al.* Self-assembly of soft nanoparticles with tunable patchiness. *Nat Nanotechnol* **4**, 721-726, doi:10.1038/nnano.2009.232 (2009).

40 Gavazzi, C. *et al.* A functional sequence-specific interaction between influenza A virus genomic RNA segments. *Proc Natl Acad Sci U S A* **110**, 16604-16609, doi:10.1073/pnas.1314419110 (2013).
41 Sugita, Y., Sagara, H., Noda, T. & Kawaoka, Y. Configuration of viral ribonucleoprotein complexes within the influenza A virion. *J Virol* **87**, 12879-12884, doi:10.1128/JVI.02096-13 (2013).
42 Shafiuddin, M. & Boon, A. C. M. RNA Sequence Features Are at the Core of Influenza a Virus Genome Packaging. *J Mol Biol*, doi:10.1016/j.jmb.2019.03.018 (2019).
43 Haralampiev, I. *et al.* Selective flexible packaging pathways of the segmented genome of influenza A virus. *Nat Commun* **11**, 4355, doi:10.1038/s41467-020-18108-1 (2020).
44 Le Sage, V. *et al.* Mapping of Influenza Virus RNA-RNA Interactions Reveals a Flexible Network. *Cell Rep* **31**, 107823, doi:10.1016/j.celrep.2020.107823 (2020).
45 Lampejo, T. Influenza and antiviral resistance: an overview. *Eur J Clin Microbiol Infect Dis* **39**, 1201-1208, doi:10.1007/s10096-020-03840-9 (2020).
46 Bruce, E. A., Digard, P. & Stuart, A. D. The Rab11 pathway is required for influenza A virus budding and filament formation. *J Virol* **84**, 5848-5859, doi:10.1128/JVI.00307-10 (2010).
47 Nakatsu, Y. *et al.* Intracellular transport of the measles virus ribonucleoprotein complex is mediated by Rab11A-positive recycling endosomes and drives virus release from the apical membrane of polarized epithelial cells. *J Virol* **87**, 4683-4693, doi:10.1128/JVI.02189-12 (2013).
48 Nanbo, A. & Ohba, Y. Budding of Ebola Virus Particles Requires the Rab11-Dependent Endocytic Recycling Pathway. *J Infect Dis* **218**, S388-S396, doi:10.1093/infdis/jiy460 (2018).
49 Cosentino, G. *et al.* Respiratory syncytial virus ribonucleoproteins hijack microtubule Rab11 dependent transport for intracellular trafficking. *PLoS Pathog* **18**, e1010619, doi:10.1371/journal.ppat.1010619 (2022).
50 Fay, M. M. & Anderson, P. J. The Role of RNA in Biological Phase Separations. *J Mol Biol* **430**, 4685-4701, doi:10.1016/j.jmb.2018.05.003 (2018).

METHODS

Cell, viruses and reagents.

GFP-Rab11a-WT and GFP-Rab11a-DN cell lines were produced in-house and characterized in [19], while the human alvelolar basal cell (A549) and epithelial cell Madin-Darby Canine Kidney (MDCK) were generous gifts from Prof Paul Digard, Roslin Institute, UK. Cells were cultured in Dulbecco´s Modified Eagle´s Medium (DMEM) supplemented with 10% fetal bovine serum (FBS), 2 mM L-glutamine and 1% Pencillin-Streptomycin. GFP-Rab11a cell lines were cultured/maintained in DMEM supplemented with 1.25 µg/mL Puromycin.

Reverse-genetics engineered A/Puerto Rico/8/34 virus (PR8 WT; H1N1) was used to infect all cell types and titrated by plaque assay in MDCK cells, while X31 virus (a reassortant virus carrying HA and NA segments from A/Hong-Kong/1/1968 (H3N2) in the background of PR8) was used to infect mice. For viral titre measurement, A549 cells were seeded for 24 hrs, infected at 3 multiplicity of infection (MOI) in DMEM supplemented with 2 mM L-glutamine and 1% penicillin/streptomycin and devoid of sera for 45 mins at 37 °C and 5% CO_2. The supernatants

were subjected to a plaque assay in MDCK cells to calculate the virus titres, as described previously [52]. Infection for live imaging were done at 10 MOI, with viral infections for immunofluorescence at an MOI of 3 or 5.

Nucleozin was dissolved in dimethyl sulfoxide (DMSO) and used at a final concentration of 2 µM (immunofluorescence staining and virus titres) or 5 µM (live imaging), while 1,6-Hexanediol was dissolved in DMEM and used at 5 % (w/v).

Animal and infection

Female C57Bl/6 mice were infected with 4000pfu of X31 (A/X31; H3N2) virus for 2 days. At 30min, 1h or 2h before the collection of the lungs, each mouse was intranasally treated with PBS (vehicle) or 2.3mg/mL of nucleozin (Ncz). Then, lungs were collected to determine viral titres by plaque assays (using MDCK infected with a set of serial dilutions from the homogenized lung tissue samples) and for histology processing.

Ethics statement

All experiments involving mice were performed using 8-week-old littermate C57BL6/6J, female mice under specific pathogen-free conditions at the Instituto Gulbenkian de Ciência (IGC) biosafety level 2 animal facility (BSL-2). Animals were group housed in individually ventilated cages with access to food and water *ad libitum*. This research project was ethically reviewed and approved by both the Ethics Committee and the Animal Welfare Body of the IGC (license reference: A003.2021), and by the Portuguese National Entity that regulates the use of laboratory animals (DGAV – Direção Geral de Alimentação e Veterinária (license references: 0421/000/000/2022, Controlling influenza A virus liquid organelles – LOFLU, funded by the European Research Council). All experiments conducted on animals followed the Portuguese (Decreto-Lei nº 113/2013) and European (Directive 2010/63/EU) legislations, concerning housing, husbandry, and animal welfare.

Western Blot

Immunoblotting was performed according to standard procedures and imaged using a LI-COR Biosciences Odyssey near-infrared platform. Antibodies used included: rabbit polyclonal antibody against NP (1:1000) and PB2 (1:500); which were kindly provided by Prof. Paul Digard, Roslin Institute, UK; goat polyclonal antibody against green fluorescent protein (GFP) (1:2000; Sicgen, AB0020), and mouse monoclonal antibody (Isotype IgG1) against actin (1:1000, Sigma-Aldrich, A5441). The secondary antibodies used were from IRDye range (1:10000; LI-COR Biosciences).

Microscopy and image processing

For immunofluorescence, cells were fixed in 4% paraformaldehyde for 10 mins and permeabilized with triton-X-100 (0.2% (v/v)), incubated in primary antibodies for 1 h at RT, washed (3x) in PBS/1% FBS and finally incubated in Hoechst and Alexa Fluor conjugated secondary antibodies for 45mins at RT. Antibodies used were rabbit polyclonal against Rab11a (1:100; Proteintech, 15903-1-AP), calnexin (1:1000, Abcam, 22595), TRIM25 (1: 100, Abcam, ab167154), and NP (1:1000; gift from Prof Paul Digard), mouse polyclonal against NS1 (Neat, in-house from hybridoma made at the IGC antibody facility), mouse monoclonal against NP (1:1000; Abcam, 20343), Tom20 (1:200; Sigma-Aldrich, WH0009804M1) and Drp1 (1:200; Abcam, ab56788). Secondary antibodies were all from the Alexa Fluor range (1:1000; Life Technologies).

Following washing in PBS, cells were mounted with Dako Faramount Aqueous Mounting Medium and single optical sections were imaged with a Leica SP5 live or stellaris confocal microscope using the photon counter mode. For z-stacks image, a spinning disk 3i (Marianas) confocal microscope was used in the super-resolution (CSU-W1, SoRa) mode. Samples were imaged on a 63x oil immersion Nikon objective (NA = 1.4). Using the function sum of slices, stacked images were projected to 2D and inclusion and its cytoplasmic milieu were segmented and analyzed using Lab-custom ImageJ macros and R analytics scripts.

Determining inclusion topology and thermodynamics

To determine the total concentration of vRNPs (NP as proxy) transported to the cytoplasm in relation to vRNPs produced in the nucleus ($\frac{Ccytoplasm}{Cnucleus}$), a sum of slices of z-stacked images were used, otherwise, single plane images were analysed for other parameters. We used a custom (Fiji Is Just) ImageJ 2.1.0/1.53p script for image processing using the following pipeline: **(1.)** Segment cell periphery. **(2.)** Segment and remove nucleus from the cell to make the cytoplasm. **(3.)** From the cytoplasm, segment inclusions **(4.)** Analyse the cytoplasm, nucleus, and inclusions for number and topological shape descriptors **(5.)** Using the appropriate segmented region, measure the mean fluorescence intensity (as proxy of concentration) of cell, nucleus, cytoplasm, and cytoplasmic inclusion (*See Fig. 1, method*).

Using the method published by Riback *et al. 2020* as template, we determined C_{dense} as the mean fluorescence intensity of the segmented inclusion while C_{dilute} was extrapolated from remaining cytoplasmic vRNP intensity outside the inclusions. Partition coefficient (K) and free energy (ΔG) were derived based on Riback *et al.,* 2020 publication; where $K = \frac{Cdense}{Cdilute}$, and $\Delta G = -RT\ln K$.

Inclusion saturation concentration (C_{sat}) is the threshold C_{dilute} where inclusion begins to appear (~ 6hpi) and is calculated as the minimum C_{dilute} in cells with observable viral inclusions. All data were normalised to 3hpi (an infection stage with nuclear vRNP staining lacking cytoplasmic inclusions); in the case of free energy, this normalization was represented as ΔΔG.

Cartesian analysis of mitochondria distribution

To quantify the mitochondria distribution, we have created an automated tool, which consists of the conversion of a confocal image from polar to Cartesian system. Upon establishing the centre of the polar coordinate as the periphery of the cell nucleus, and circulating clockwise, we display the signal of each channel one degree apart in a XY graph. The analysis continues repeating the process upon increments of a fixed width, towards the cell surface. The organelle distribution map in this format provides means to accurately quantify polarization, redistribution towards the perinuclear region or expansion to the cell periphery, thus allowing a systematic analysis. The automated system is powerful because it allows to image and process a statistically significant number of cells using the indicated procedure.

Live Imaging, photoactivation

A549 cells were seeded in 8-well glass-bottomed dish (Ibidi) and grown overnight in OptiMEM (37ºC, 5% CO_2). Cells infected with PR8 at an MOI of 10 were transfected simultaneously with 200ng/µl GFP-NP or cherry-NP plasmid. For photoactivation experiment, a corresponding plasmid of either photoactivatable cherry-NP or photoactivatable GFP-NP was co-transfected with lipofectamine LTX. Cells were imaged using OptiMEM or Leibovitz medium with a 63x oil immersion Nikon objective (NA = 1.4) on Roper TIRF, AiryScan or spinning disk confocal (SoRa) microscopes equipped with temperature (37ºC) and CO_2 (5%) regulated chamber and stage. Inclusions at a specified region of interest (ROI) was activated by blue light (405 nm laser) at 100% intensity and imaged at 1 frame/ sec for 2 min using 488 nm and 568 nm lasers for GFP and cherry respectively. Photoactivation data were post-processed in FIJI (Image J) using a modified FLAPh algorithm and analysed with a lab-custom R script. Model was obtained using single exponential curve fitting. $y = (1-a) + ae^{-kt}$, a = mobile fraction, K = decay rate constant (per second, s^{-1}), t = time (s).

Particle tracking and coarsening assay

Trackmate plugin ((Fiji Is Just) ImageJ 2.1.0/1.53p, FIJI) was used to track inclusions at a timescale of 1 s/frame in live imaging samples and XY trajectories were subsequently analysed

in a custom R (version 4.1.0) script. Using (FIJI and R), coarsening assay was analysed from time-lapsed tracking of two inclusions, starting from the point they first touch to the point they relax into a rounded puncta with an aspect ratio (AR) of 1.

Statistical analysis

After testing for homogeneity of variance, homogenously distributed data were assessed by parametric test using One-way ANOVA, followed by Tukey multiple comparisons of means. In contrast, non-homogenous data were assessed by non-parametric test with statistical levels determined after Kruskal-Wallis Bonferroni treatment. Alphabets above each boxplot represents the statistical differences between groups. Same alphabets indicate lack of significant difference between groups while different alphabets infer a statistically significant difference at $\alpha = 0.05$.

Solubility Proteome Profiling

A549, GFP-Rab11a-WT and GFP-Rab11a-DN cells were mock-infected or infected with PR8 virus between 4 to 16hpi and treated with nucleozin or DMSO. Frozen cell pellets containing $1x10^6$ cells were shipped to Proteomics Core Facility at EMBL, Heidelberg for further sample processing.

Samples for mass spectrometry analysis were prepared as described [53]. Briefly, $1x10^6$ cells were resuspended in 100 µl lysis buffer (0.8 % NP-40, 1x cOmplete protease inhibitor cocktail (Roche), 1x PhosphoStop (Roche), 1 U/ml RNAsin (Promega), 1.5 mM $MgCl_2$ in PBS (2.67 mM KCl, 1.5 mM KH2PO4, 137 mM NaCl, and 8.1 mM NaH2PO4, pH 7.4). The sample aliquot for total proteome was incubated directly with benzonase on ice, while the sample aliquot for the soluble proteome was spun down at 100,000 g at 4 °C for 20 min. The supernatant was incubated with benzonase. Both total and soluble aliquots were incubated for 10 min with final 1 % SDS. Protein concentration was determined for the total proteome sample and aliquots equal to 5 µg protein were taken for sample preparation for MS analysis. Both soluble and total lysate of each sample was combined in a multiplexing MS experiment.

Mass spectrometry sample preparation

Sample preparation for mass spectrometric measurements were performed as described in [28,54] .

Protein digestion and labelling

Protein digestion was performed using a modified SP3 protocol [55,56]. 5 µg of proteins (per condition) were diluted to a final volume of 20 µl with 0.5% SDS and mixed with a bead slurry

(Sera-Mag Speed beads, Thermo Fisher Scientific) in ethanol) and incubated on a shaker at room temperature for 15 min. The beads were washed four times with 70% ethanol. Proteins on beads were overnight reduced (1.7mM TECP), alkylated (5mM chloroacetamide) and digested (0.2 µg trypsin, 0.2µg LysC) 100 mM HEPES, pH8. On the next day, peptides were eluted from the beads, dried under vacuum, reconstituted in 10 µl of water and labelled with TMT-16plex reagents for one hour at room temperature. The labelling reaction was quenched with 4 µl of 5% hydroxylamine and the conditions belonging to a single MS experiment were pooled together. The pooled sample was desalted with solid-phase extraction after acidification with 0.1 % formic acid. The samples were loaded on a Waters OASIS HLB µelution plate (30µm), washed twice with 0.05% formic acid and finally eluted in 100 µl of 80% acetonitrile containing 0.05% formic acid. The desalted peptides were dried under vacuum and reconstituted in 20 mM ammonium formate. The samples were fractionated using C18-based reversed-phase chromatography running at high pH. Mobile phases constituted of 20 mM Ammonium formate pH 10 (buffer A) and acetonitrile (buffer B). This system was run at 0.1 ml/min on the following gradient: 0% B for 0 – 2 min, linear increase 0 - 35% B in 2 – 60 min, 35 – 85% B in 60 – 62 min, maintain at 85% B until 68 min, linear decrease to 0% in 68 – 70 min and finally equilibrated the system at 0% B until 85 min. Fractions were collected between 2 – 70 min and every 12th fraction was pooled together and vacuum dried.

LC-MS-MS measurement

Samples were re-suspended in 0.05% formic acid, 4% ACN in LC-MS grade water and analyzed on Q Exactive Plus mass spectrometer (Thermo Fisher Scientific) connected to UltiMate 3000 RSLC nano system (Thermo Fisher Scientific) equipped with a trapping cartridge (Precolumn; C18 PepMap 100, 5 µm, 300 µm i.d. × 5 mm, 100 Å) and an analytical column (Waters nanoEase HSS C18 T3, 75 µm × 25 cm, 1.8 µm, 100 Å) for chromatographic separation. Mobile phase constituted of 0.1% formic acid in LC-MS grade water (Buffer A) and 0.1% formic acid in LC-MS grade acetonitrile (Buffer B). The peptides were loaded on the trap column (30 µl/min of 0.05% trifluoroacetic acid in LC-MS grade water for 3 min) and eluted using a gradient from 2 % to 30 % Buffer B over 103 min at 0.3 µl/min (followed by an increase to 40 % B, and a final wash to 80 % B for 2 min before re-equilibration to initial conditions). The outlet of the LC- system was directly fed for MS analysis using a Nanospray-Flex ion source and a Pico-Tip Emitter 360 µm OD × 20 µm ID; 10 µm tip (New Objective). The mass spectrometer was operated in positive ion mode. The spray voltage and capillary temperature was set to 2.2 kV and 275°C respectively. Full-scan MS spectra with a mass range of 375–1,200 m/z were acquired in profile mode using a resolution

of 70,000 (maximum fill time of 250 ms or a maximum of 3e6 ions (automatic gain control, AGC)). Fragmentation was triggered for the top 10 peaks with charge 2–4 on the MS scan (data-dependent acquisition) with a 30-s dynamic exclusion window (normalized collision energy was 30), and MS/MS spectra were acquired in profile mode with a resolution of 35,000 (maximum fill time of 120 ms or an AGC target of 2e5 ions).

Protein identification and quantification

The MS data was processed as described in [28]. Briefly, the raw MS data was processed with isobarQuant (and identification of peptides and proteins was performed with Mascot 2.4 (Matrix Science) against a database containing *Homo sapiens* Uniprot FASTA ((proteome ID: UP000005640, downloaded on 14 May 2016) and Influenza A virus (strain A/Puerto Rico/8/1934 H1N1, proteome ID: UP000009255) along with known contaminants and the reverse protein sequences (search parameters: trypsin; missed cleavages 3; peptide tolerance 10 ppm; MS/MS tolerance 0.02 Da; fixed modifications included carbamidomethyl on cysteines and TMT16plex on lysine; variable modifications included acetylation of protein N-terminus, methionine oxidation and TMT16plex on peptide N-termini).

Mass spectrometry data analysis and normalization.

All MS data analysis was performed using R studio (version 1.2.1335 and R version 3.6.1). Data normalization of NP40- and SDS- derived proteomes was performed with *vsn* [57]. The overall signal sum intensities distributions from all TMT channels of all replicates were corrected for technical variations.

Differential analysis of protein abundance

The $\log_2$ transformed *vsn* normalized SDS-derived signal sum intensities of proteins from different samples were analysed for differential abundances using *limma* [58]. Proteins with $|\log_2(\text{fold change})| > 0.5$ and adjusted p-value (Benjamini Hochberg) < 0.1 were considered significantly changed.

Differential analysis of protein solubility

Solubility is defined as the ratio of NP40- and SDS- derived abundances of proteins. This ratio was computed for all proteins measured in a dataset. The log2 transformed protein solubility was compared between different conditions (time points of infection or different cell line at 12 hours post infection) using *limma*. Proteins with $|\log_2(\text{fold change})| > 0.5$ and adjusted p-value (Benjamini Hochberg) < 0.1 were considered significantly changed.

Gene ontology over representation analysis

Differential abundant or soluble human proteins from infection time course or different cell line datasets were used for GO term "Biological processes" and/or "Cellular Compartments" overrepresentation analysis using clusterProfiler (R Bioconductor) [59]. All identified proteins in each dataset served as the background. Standard settings were used for representing enriched GO terms (p-value cutoff: 0.05, Benjamini-Hochberg procedure for multiple testing adjustment and q-value cutoff of 0.2).

REFERENCE METHODS

51 Snead, W. T. & Gladfelter, A. S. The Control Centers of Biomolecular Phase Separation: How Membrane Surfaces, PTMs, and Active Processes Regulate Condensation. *Mol Cell* **76**, 295-305, doi:10.1016/j.molcel.2019.09.016 (2019).

52 Matrosovich, M., Matrosovich, T., Garten, W. & Klenk, H. D. New low-viscosity overlay medium for viral plaque assays. *Virol J* **3**, 63, doi:10.1186/1743-422X-3-63 (2006).

53 Zhang, X. *et al.* Molecular mechanisms of stress-induced reactivation in mumps virus condensates. *bioRxiv*, 2021.2007.2010.451879, doi:10.1101/2021.07.10.451879 (2022).

54 Mateus, A. *et al.* The functional proteome landscape of Escherichia coli. *Nature* **588**, 473-478, doi:10.1038/s41586-020-3002-5 (2020).

55 Hughes, C. S. *et al.* Ultrasensitive proteome analysis using paramagnetic bead technology. *Mol Syst Biol* **10**, 757, doi:10.15252/msb.20145625 (2014).

56 Hughes, C. S. *et al.* Single-pot, solid-phase-enhanced sample preparation for proteomics experiments. *Nat Protoc* **14**, 68-85, doi:10.1038/s41596-018-0082-x (2019).

57 Huber, W., von Heydebreck, A., Sultmann, H., Poustka, A. & Vingron, M. Variance stabilization applied to microarray data calibration and to the quantification of differential expression. *Bioinformatics* **18 Suppl 1**, S96-104, doi:10.1093/bioinformatics/18.suppl_1.s96 (2002).

58 Ritchie, M. E. *et al.* limma powers differential expression analyses for RNA-sequencing and microarray studies. *Nucleic Acids Res* **43**, e47, doi:10.1093/nar/gkv007 (2015).

59 Yu, G., Wang, L. G., Han, Y. & He, Q. Y. clusterProfiler: an R package for comparing biological themes among gene clusters. *OMICS* **16**, 284-287, doi:10.1089/omi.2011.0118 (2012).

Reporting summary Further information on research design is available in the Nature Research Reporting Summary linked to this paper.

Data availability All experimental data shown in Figs. 1–4 and Extended Data Figs. 1–7 is available from the corresponding authors upon request. Sequences of described viruses are accessible from the NCBI virus under accession number GCF_000865725.1. Source data are provided with this paper in 10.5281/zenodo.6901207. The mass spectrometry proteomics data

have been deposited to the ProteomeXchange Consortium via the PRIDE (PubMed ID: 34723319) partner repository with the dataset identifier PXD034778.
Reviewer account details:
Username: reviewer_pxd034778@ebi.ac.uk
Password: BPrURfLw

Code availability All computer code or algorithm used to generate the results reported in the paper are available at 10.5281/zenodo.6901207.

Acknowledgements: This project has received funding from the European Research Council (ERC) under the European Union's Horizon 2020 research and innovation programme (grant agreement No. 101001521). The part of mitochondrial analysis was funded by the project grant from Fundação para a Ciência e a Tecnologia (FCT) with reference PTDC/BIA-CEL/32211/2017. Salary support from FCT : T.A.E, D.B., V.M. are funded by PhD fellowships (PD/BD/128436/2017 and COVID/BD/151646/2021), S.V.C and M.A. by D.L. 57, MJA by CEEC Ref CEECIND/02373/2020.

Author contributions: T.A.E., S.S., S.V.C, D.B., I.B., V.M., F.F., M.A, M.S., M.J.A designed and executed experiments and analysed the data. T.A.E AND M.J.A wrote the manuscript. M.J.A. initiated and designed the overall project. S.S., I.B., and M.S. designed, performed, and analysed the experiments of whole proteome solubility assay and T.A.E, D.B., S.V.C, F.F., M.A, M.J.A designed and executed experiments to validate hits. D.B., and M.J.A designed, performed, and analysed animal experiments. T.A.E., V.M., M.J.A designed, performed, and analysed the framework on how the thermodynamic variables influence biophysical parameters and implemented the framework for analyses. T.A.E, S.V.C, M.J.A., designed, performed, and analyzed all live cell analyses. M.S and M.J.A. obtained funding for the study. All authors reviewed the manuscript.

Competing interests None.

Additional information Supplementary information. The online version contains supplementary material available at ADD. Correspondence and requests for materials should be addressed to M.J.A. Peer review information Nature thanks the anonymous reviewers for their contribution to the peer review of this work. Reprints and permissions information is available at http://www.nature.com/reprints.

EXTENDED MATERIAL

This section contains extended material – Supplementary Videos 1-10, Supplementary Tables 1-8 Extended Data Figures 1-7, - for the manuscript “influenza A virus liquid condensates may be selectively hardened by compounds stabilizing intersegment interactions” from the authors Temitope Akhigbe Etibor, Sindhuja Sridharan, Sílvia Vale-Costa, Daniela Brás, Isabelle Becher, Victor Mello, Filipe Ferreira, Marta Bebiano Alenquer, Mikhail Savitski and Maria João Amorim.

Supplementary Videos

All videos were acquired at the speed of 1second/frame.

Supplementary Video 1: Fusion and Fission dynamics of IAV inclusions with endogenous Rab11a.

A549 cells expressing endogenous Rab11a were PR8 infected and co-transfected with cherry-NP for 16 hrs and subsequently monitored for inclusion fusion and fission events by live imaging.

Supplementary Video 2: Fusion and Fission dynamics of IAV inclusions overexpressing Rab11a.

Cell lines overexpressing Rab11a-WT were PR8 infected and co-transfected with cherry-NP for 16 hrs, after which fusion and fusion dynamics were monitored by live imaging.

Supplementary Video 3: Coarsening assay in liquid inclusions

Liquid-like DMSO-treated inclusions formed in post infected and GFP-NP co-transfected A549 cells were quantified for their ability to coarsen by live imaging. We present 2 videos a-b, showing an entire cell (a) or an inlet with an example of fusion event (b).

Supplementary Video 4: Coarsening assay in Solid-like inclusions

Hardened nucleozin-induced inclusions formed in post infected and GFP-NP co-transfected A549 cells were quantified for their inability to coarsen by live imaging. We present 2 videos a-b, showing an entire cell (a) or an inlet with an example of fusion event (b).

Supplementary Video 5: Fluorescence loss after photoactivation (FLAPh) in liquid inclusions.

PR8 infected A549 was co-transfected with cherry-NP and photoGFP-NP and treated with DMSO for posterior photoactivation of viral inclusions (with blue light, 405 nm) at a region of interest (ROI). Fluorescence loss in the ROI was monitored over time as vRNPs (NP, as a proxy) were transferred from the activated zone to the inactivated region. We present 3 videos a-d, the separate channels for cherry-NP (a), photoGFP-NP (b), the merged video (c).

Supplementary Video 6: Fluorescence loss after photoactivation (FLAPh) in hardened inclusions.

PR8 infected A549 was co-transfected with photoGFP-NP and cherry-NP and treated with nucleozin for posterior photoactivation of viral inclusions (with blue light, 405 nm) at a region of interest (ROI). Fluorescence loss in the ROI was monitored over time as vRNPs (NP, as a

proxy) were transferred from the activated zone to the inactivated region. We present 3 videos a-c, the separate channels for cherry-NP (a), photoGFP-NP (b), the merged video (c).

Supplementary Video 7: Fluorescence recovery after photobleaching (FRAP) in liquid inclusions

PR8 infected A549 co-transfected with GFP-NP and cherry-NP were treated with nocodazole (Noc) and subsequently photobleached (488 nm) at a region of interest (ROI) in the centre of an inclusion to follow the internal rearrangement by live imaging. We present 2 videos a-b, showing an entire cell (a) or an inlet with an example of fusion event (b).

Supplementary Video 8: FRAP in hardened inclusions.

PR8 infected A549 co-transfected with GFP-NP and cherry-NP were treated with both nocodazole and nucleozin and subsequently photobleached (488 nm) at a region of interest (ROI) in the centre of an inclusion to see if internal rearrangement occurred during live imaging. We present 2 videos a-b, showing an entire cell (a) or an inlet with an example of fusion event (b).

Supplementary Video 9: Coarsening assay of Rab11a-DN cells treated with DMSO but lacking inclusions.

GFP-Rab11a-DN cell lines lacking viral inclusion and coarsening events upon infection and transfection (cherry-NP). We present 4 videos a-d, the separate channels for cherry-NP (a), photoGFP-NP (b), the merged video (c).

Supplementary Video 10: Coarsening assay of hardened viral inclusions formed by treating Rab11a-DN with nucleozin.

GFP-Rab11a-DN cell lines transfected (with cherry-NP) and PR8-infected display a solid-like coarsening behaviour when treated with nucleozin. We present 4 videos a-d, the separate channels for cherry-NP (a), photoGFP-NP (b), the merged video (c).

Supplementary Tables

Supplementary Table 1: Topology,thermodynamics and material properties of IAV inclusions.

After PR8 infection (1 MOI) inclusions were subjected to thermal changes (Sheet 1) and live imaging for inclusion tracking (Sheet 4), fusion dynamics (Sheet 5) and FLAPh (Sheet 6), or observed for different hours post infection (hpi) (Sheet 2), or nucleozin treatment (Sheet 3). The data summary of inclusion topology and thermodynamics are listed in this table in sheet 1-3. Mice was infected with X31 and treated with PBS or nucleozin for the analysis of number of inclusion and topology in lung slices (Sheet 7).

Supplementary Table 2: Differential analysis of protein abundance changes along the infection time course

A549 cells were infected with PR8 for 4, 8, 12 and 16 hours. The changes in protein abundances (of both host and virus) along the infection time course was compared to non-infected cells in a proteome-wide scale are listed in this table.

Supplementary Table 3: Differential analysis of protein solubility changes along the infection time course

A549 cells were infected with PR8 for 4, 8, 12 and 16 hours. The changes in protein solubility (NP40/SDS ratio of both host and virus) along the infection time course was compared to non-infected cells in a proteome-wide scale are listed in this table.

Supplementary Table 4: Hierarchical clustering of the solubility hits along the infection time course

Solubility profiles of proteins showing significant alteration (see methods) in solubility along the infection course (from supplementary table 2) were clustered using into 6 distinct patterns.

Supplementary Table 5: Differential analysis of protein abundance changes at 12 hours post infectionhpi in Rab11a-WT and Rab11a-DN cell lines

Rab11a-WT and Rab11a-DN cells were infected with PR8 IAV for 12 hours. Protein abundances (of both host and virus) changes occurring in Rab11a-DN cells compared to Rab11a-WT on a proteome-wide scale are listed in this table.

Supplementary Table 6: Differential analysis of protein solubility changes at 12 hours post infection in WT and Rab11a-DN cell lines

Rab11a-WT and Rab11a-DN cells were infected with PR8 IAV for 12 hours. Protein solubility (of both host and virus) changes occurring in Rab11a-DN cells compared to Rab11a-WT on a proteome-wide scale are listed in this table.

Supplementary Table 7: Differential analysis of protein solubility changes before and after nucleozin treatment at 12 hours post infection in WT and Rab11a-DN cell lines

PR8-infected Rab11a-WT and Rab11a-DN cells were treated with either DMSO (vehicle) or 5 µM of nucleozin for 1 hour. The protein solubility changes upon nucleozin (or DMSO) treatment in RAB11a-WT and Rab11a-DN cells is listed in this table.

Supplementary Table 8: Differential analysis of protein abundance changes before and after nucleozin treatment at 12 hours post infection in WT and Rab11a-DN cell lines

PR8-infected Rab11a-WT and Rab11a-DN cells were treated with either DMSO (vehicle) or 5 µM of nucleozin for 1 hour. The protein abundance changes upon nucleozin (or DMSO) treatment in RAB11a-WT and Rab11a-DN cells is listed in this table.

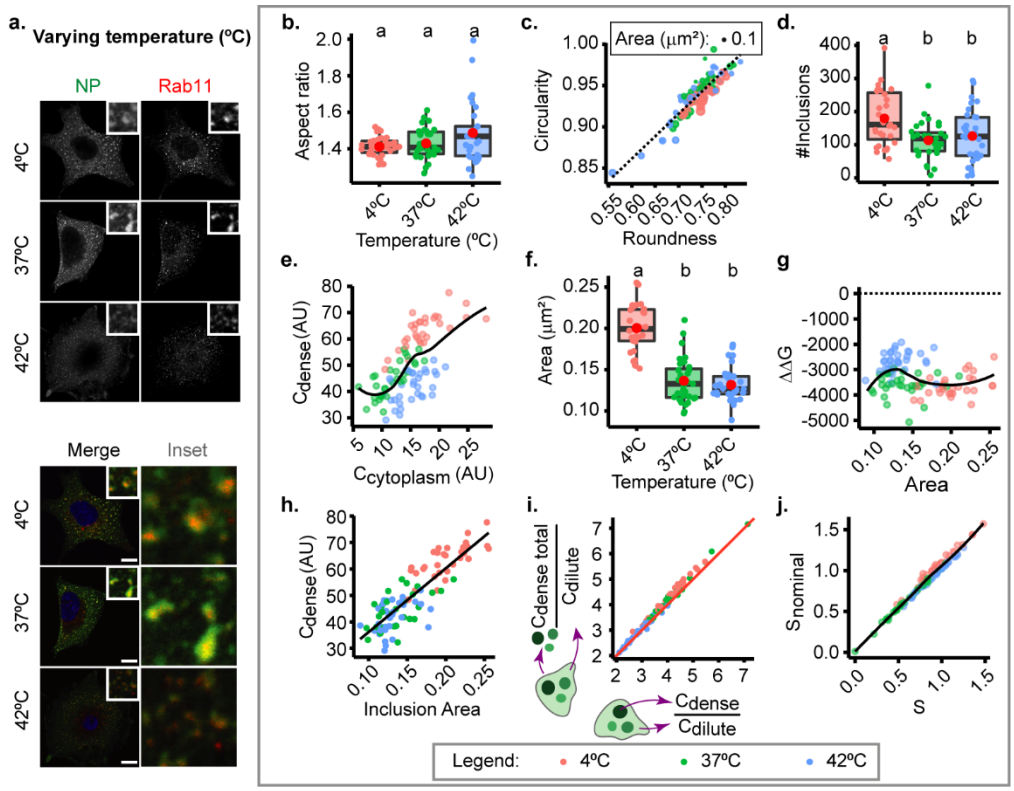

Extended Data Fig. 1: Temperature changes confer a modest alteration to inclusions properties. A549 were infected at a multiplicity of infection of 3 with PR8 virus for 8 hrs, incubated at different temperatures (4ºC, 37ºC, 42ºC), fixed and stained for NP (as proxy for vRNP) by immunofluorescence. The biophysical parameters (**b. - j.**) were extracted from images of fixed infected cells measuring NP intensity (as a proxy for vRNPs, n = 18 - 29). We adapted the method published by [16] to determine concentration C_{dense} as the mean fluorescence intensity of vRNPs in the segmented IAV inclusions, while concentration C_{dilute} was extrapolated from the cytoplasmic vRNP intensity outside the inclusions. Each dot is the average value of measured parameter within or outside IAV inclusions per cell, while the continuous black lines are non-linear fitted models for all data. In (**i.**), conditions were normalized to an infection state without IAV inclusions (3 hpi at 37ºC) that is indicated by the dashed black line. Above each boxplot, same letters indicate no significant difference between them, while different letters indicate a statistical significance at α = 0.05. Abbreviations: AU, arbitrary unit. **a.** Immunofluorescence images of fixed A549 cells infected showing alterations to inclusions at different temperatures (ºC). **b.** Boxplot of aspect ratio of inclusions at different temperature (ºC); P = 0.234; Kruskal Wallis Bonferroni treatment. **c.** Scatter plot of inclusions circularity versus roundness at different temperatures (ºC). **d.** Boxplot showing number of inclusions per cell at different temperatures (ºC); P = 0.00118; one-way ANOVA, followed by Tukey multiple comparisons of means. **e.** Scatter plot of vRNP concentration within inclusions (C_{dense}, AU) versus its total cytoplasmic vRNP concentration ($C_{cytoplasm}$, AU) at different temperatures (ºC). **f.** Boxplot of inclusion area per cell at different temperatures (ºC); $P < 0.00387$; Kruskal Wallis Bonferroni treatment. **g.** Scatter plot of relative fold change in free energy of partition (ΔΔG) versus area of inclusion at different temperatures (ºC). **h.** Scatter

plot of vRNP concentration in inclusion (C_{dense}, AU) versus area of inclusion at different temperatures (ºC). To validate the method for calculating partition coefficient and degree of supersaturation relative to its application in other manuscripts, we compared different methods to calculate the C_{dilute}, C_{dense}, S, and $S_{nominal}$ (**i. – j.**). **i.** Scatter plot showing the relationship between partition coefficient ($K = \frac{Cdense}{Cdilute}$) derived from average inclusion vRNP concentration ($C_{dense\ total}$) in all inclusion per cell vs partition coefficient (K) calculated from the vRNP concentration (C_{dense}) of individual inclusions in each cell at different temperatures (ºC). **j.** Scatter plot of norminal degree of supersaturation ($S_{nominal} = \mathit{In}\ \frac{Ctotal}{Csat}$) versus degree of supersaturation ($S = \mathit{In}\ \frac{Cdilute}{Csat}$) at different temperaturess (ºC). C_{Sat} is calculated as the minimum C_{dilute} in cells with observable viral inclusions.

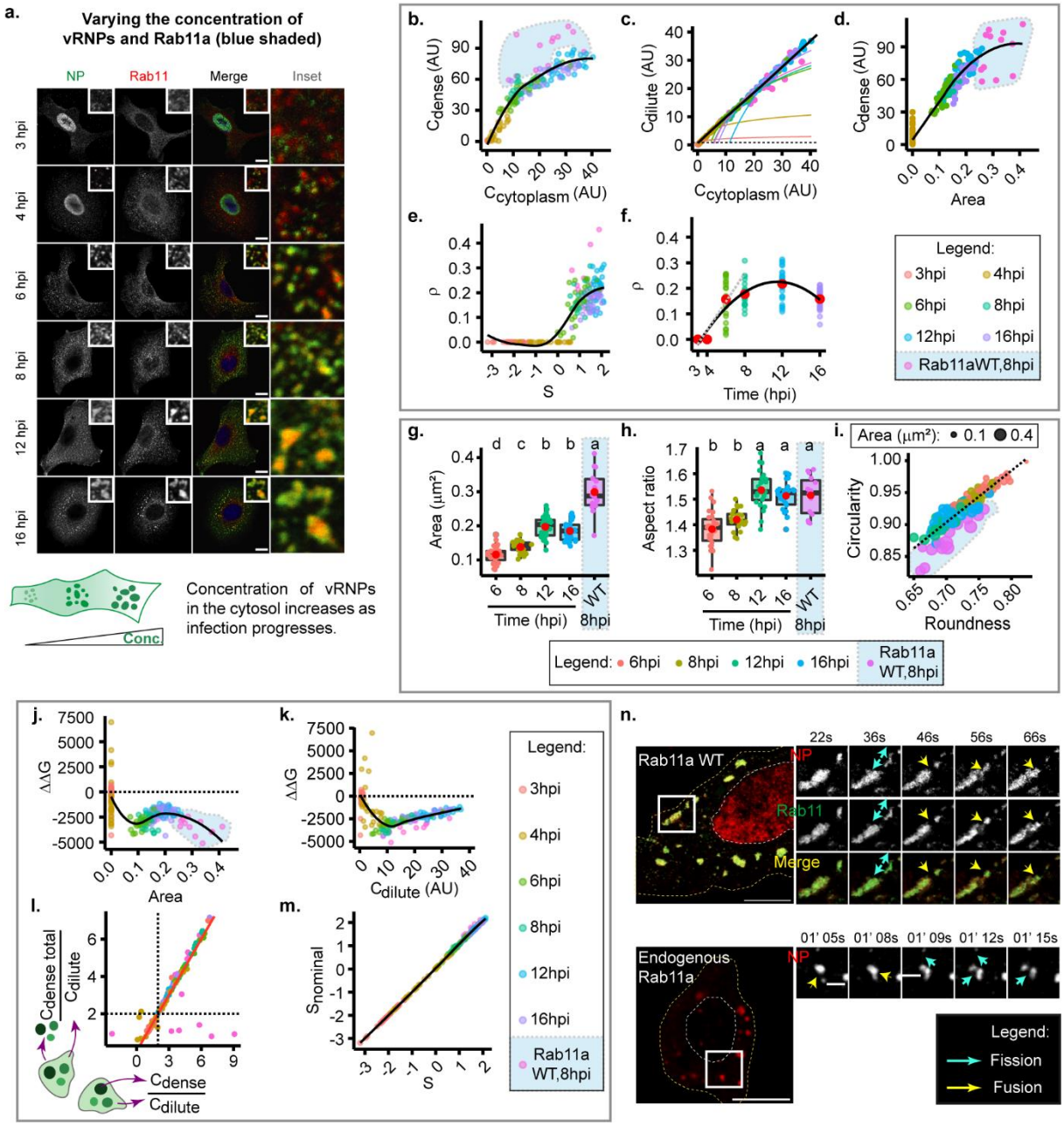

Extended Data Fig. 2: Concentration changes modestly alters to inclusions properties. Cells (A549 or GFP-Rab11-WT) were infected at a multiplicity of infection (MOI) of 3 with PR8 virus and, at the indicated time points, were fixed and stained for NP by immunofluorescence (**a. - m.**). For live imaging (**n.**), A549 cells were co-transfected with a plasmid encoding Rab11a-WT and mCherry-NP and simultaneously infected with PR8 virus at an MOI of 10 and were live imaged at 12hpi. The cytoplasmic vRNP concentration increases with time of infection (hpi) and was used as a proxy for cytoplasmic vRNP concentration changes. (**b. – m.**) We adapted the method published by [16] to determine concentration C_{dense} as the mean fluorescence intensity of vRNPs in the segmented IAV inclusions, while concentration C_{dilute} was extrapolated from the cytoplasmic vRNP intensity outside the inclusions. Also, size and shape of inclusion

was extracted from the segmented inclusions. Each dot is the average value of measured parameter within or outside IAV inclusions per cell, while the continuous black lines are non-linear fitted models for all data. Conditions were normalized to an infection state without IAV inclusions (3 hpi) that is indicated by the dashed black line. Above each boxplot, same letters indicate no significant difference between them, while different letters indicate a statistical significance at α = 0.05 using one-way ANOVA, followed by Tukey multiple comparisons of means for parametric analysis, or Kruskal-Wallis Bonferroni treatment for non-parametric analysis. Abbreviations: AU, arbitrary unit, and WT, Rab11a-WT. **a.** Immunofluorescence images of infected and fixed A549 cells at different times post-infection (hpi, a proxy for changing cytoplasmic vRNP concentration); NP (green), Rab11 (red), and nucleus (blue). Scale bar = 10 µm. **b.** Scaterr plot of vRNP concentration withing inclusions (C_{dense} - AU) and its total cytoplasmic vRNP concentration ($C_{cytoplasm}$, AU). **c.** Scatter plot of vRNP concentration outside inclusions (C_{dilute}, AU) versus total cytoplasmic vRNPs concentration ($C_{cytoplasm}$, AU) with time of infection. Coloured lines are non-linear fitted models of the data points in the graph. **d.** Scatter plot of (C_{dense}, AU) in free energy or partition (ΔΔG) versus area of inclusion. **e.** Scatter plot showing nucleation density ($\rho = \frac{number\ of\ inclusion}{Cytoplasm\ Area}$, μm^{-2}) versus degree of supersaturation ($S = \mathit{In}\ \frac{Cdilute}{Csat}$) at different time of infection. **f.** Dot plot and model depicting nucleation density (ρ) over time of infection (hpi). **g.** Boxplot of inclusion area per cell at different post-infection time (hpi). $P = 0$; Kruskal Wallis Bonferroni treatment. **h.** Boxplot of inclusion aspect ratio at different hours post-infection (hpi). $P < 2e\text{-}16$; one-way ANOVA, followed by Tukey multiple comparisons of means. **i.** Scatter plot of inclusion circularity versus roundness at different time post infection (hpi). **j.** Scatter plot of fold change in free energy of partition (ΔΔG) relative to 3hpi versus area of inclusion. **k.** Scatter plot of fold change in free energy of partition (ΔΔG, where $\Delta G = -RT\mathit{In}K$, and $K = \frac{Cdense}{Cdilute}$)versus C_{dilute} (AU) with time of IAV infection. To validate the method for calculating partition coefficient and degree of supersaturation relative to its application in other manuscripts, we compared different methods to calculate the C_{dilute}, C_{dense}, S, and $S_{nominal}$ (**l. – m.**). **l.** Scatter plot of partition coefficient (K) derived from averaged vRNP concentration in all inclusion per cell ($C_{dense\ total}$, AU) versus partition coefficient calculated from vRNP concentration from individual inclusion (C_{dense}, AU) in each cell at different time post infection (hpi). **m.** Scatter plot of nominal degree of supersaturation ($S_{nominal} = \mathit{In}\ \frac{Ctotal}{Csat}$) versus degree of supersaturation ($S = \mathit{In}\ \frac{Cdilute}{Csat}$) at different time post infection (hpi). **n.** Time lapse image of fission (blue arrow) and fusion (yellow arrow) dynamics of viral inclusions at 16hpi in cells expressing endogenous and overexpressed Rab11a (Supplementary Video 9,10).

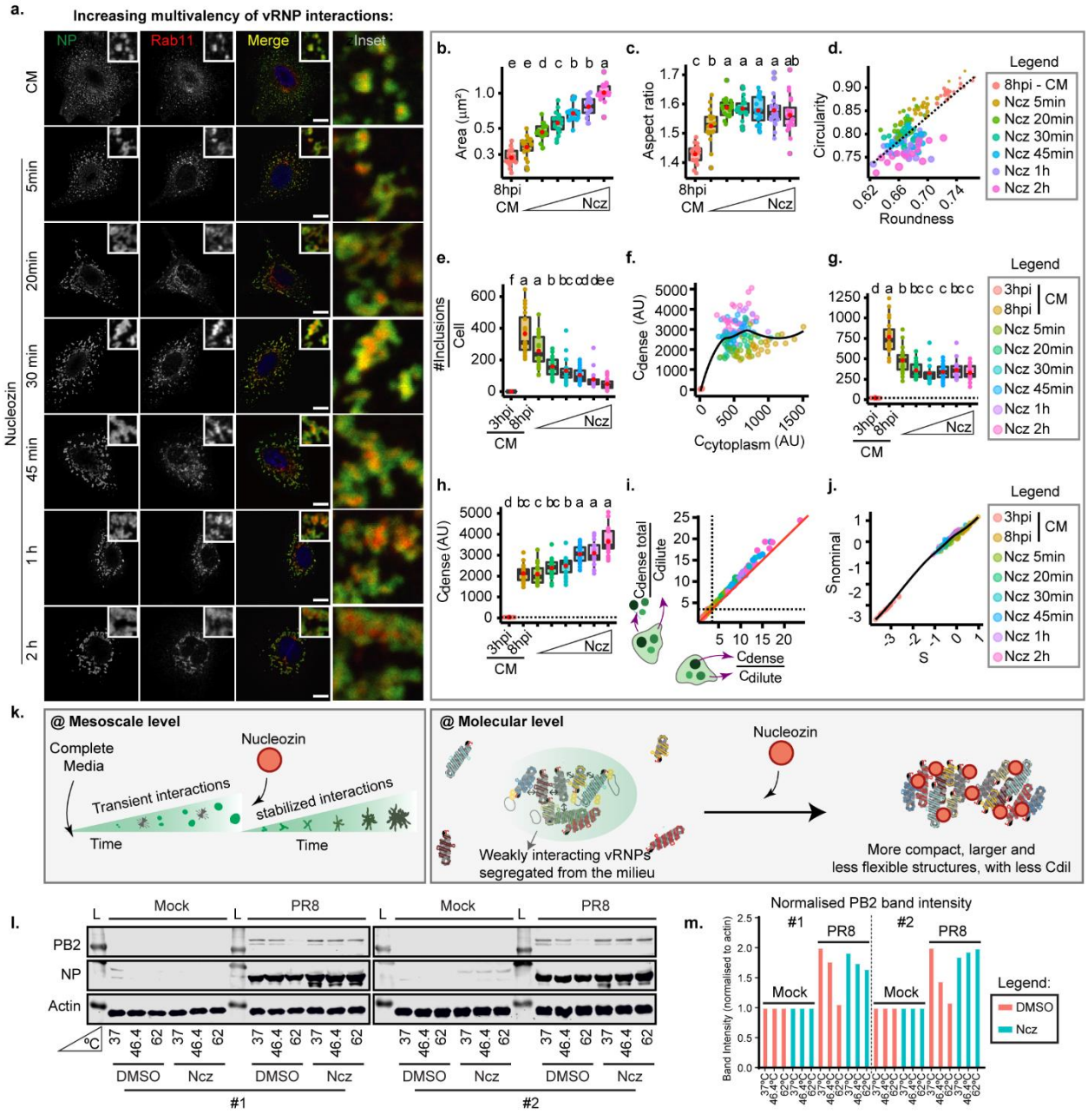

Extended Data Fig. 3: Increased interaction number and strength IAV inclusions. (a. - k.) A549 cell were infected at a multiplicity of infection (MOI) of 3 with PR8 virus for 8 hrs, then incubated with nucleozin (Ncz) for 5mins - 2hrs before fixing and staining for NP and Rab11 by immunofluorescence. (**b. – j.**) We adapted the method published by [16] to determine concentration C_{dense} as the mean fluorescence intensity of vRNPs in the segmented IAV inclusions, while concentration C_{dilute} was extrapolated from the cytoplasmic vRNP intensity outside the inclusions. Also, size and shape of inclusion was extracted from the segmented inclusions. Each dot is the average value of measured parameter within or outside IAV inclusions per cell,

while the continuous black lines are non-linear fitted models for all data. In (**i. – j.**), conditions were normalized to an infection state without IAV inclusions (3 hpi) that is indicated by the dashed black line. Above each boxplot, same letters indicate no significant difference between them, while different letters indicate a statistical significance at α = 0.05 using one-way ANOVA, followed by Tukey multiple comparisons of means for parametric analysis, or Kruskal-Wallis Bonferroni treatment for non-parametric analysis. Abbreviations: AU, arbitrary unit, and WT, Rab11a-WT, CM, complete media and Ncz, nucleozin. **a.** Immunofluorescence images of A549 cells infected and fixed before and after Ncz treatment. NP (green), Rab11a (red). Scale bar = 10µm. **b.** Boxplot of inclusion area per cell before and after Ncz treatment. *P* = 0; Kruskal Wallis Bonferroni treatment. **c.** Boxplot of inclusion aspect ratio before and after nucleozin (Ncz) treatment. *P* < 2e-16; Kruskal Wallis Bonferroni treatment. **d.** Scatter plot of inclusion circularity versus roundness before and after Ncz treatment. **e.** Boxplot showing the number of inclusions per cell before before and after Ncz treatment. *P* = 0; Kruskal Wallis Bonferroni treatment. **f.** Scatter plot of vRNP concentration within inclusions (C_{dense}, AU) and its total cytoplasmic vRNP concentration ($C_{cytoplasm}$, AU) before and after Ncz treatment. **g.** Boxplot showing inclusion C_{dilute} (AU) drop till 20min of Ncz resident time after which it plateaus. *P* = 0; Kruskal Wallis Bonferroni treatment. **h.** Boxplot showing increasing inclusion C_{dense} (AU) with increasing Ncz residence time. *P* = 0; Kruskal Wallis Bonferroni treatment. To validate the method for calculating partition coefficient and degree of supersaturation relative to its application in other manuscripts, we compared different methods to calculate the C_{dilute}, C_{dense}, S, and $S_{nominal}$ (**i. – j.**). **i.** Scatter plot of partition coefficient (K) derived from average vRNP concentration in all inclusions ($C_{dense\ total}$, AU) per cell vs partition coefficient calculated from individual vRNP concentration of each inclusion (C_{dense}, AU) per cell before and after Ncz treatment. **j.** Scatter plot of norminal degree of supersaturation ($S_{nominal} = ln\ \frac{Ctotal}{Csat}$) versus degree of supersaturation ($S = ln\ \frac{Cdilute}{Csat}$) before and after Ncz treatment. **k.** Graphical abstract depicting the hardening effects of Ncz on vRNPs and mesoscale inclusions. **(l.- m.)** A549 cell were infected at a multiplicity of infection (MOI) of 3 with PR8 virus or mock-infected for 12 hrs, incubated with 5µM Ncz or vehicle (DMSO) for 30mins, then subjected to heat ranging from 37ºC to 62ºC (for 7mins) before collecting lysates in Laemlli´s buffer. **l.** Western blot showing the PB1, NP and actin bands. **m.** Band quantification of PB1 normalised to control.

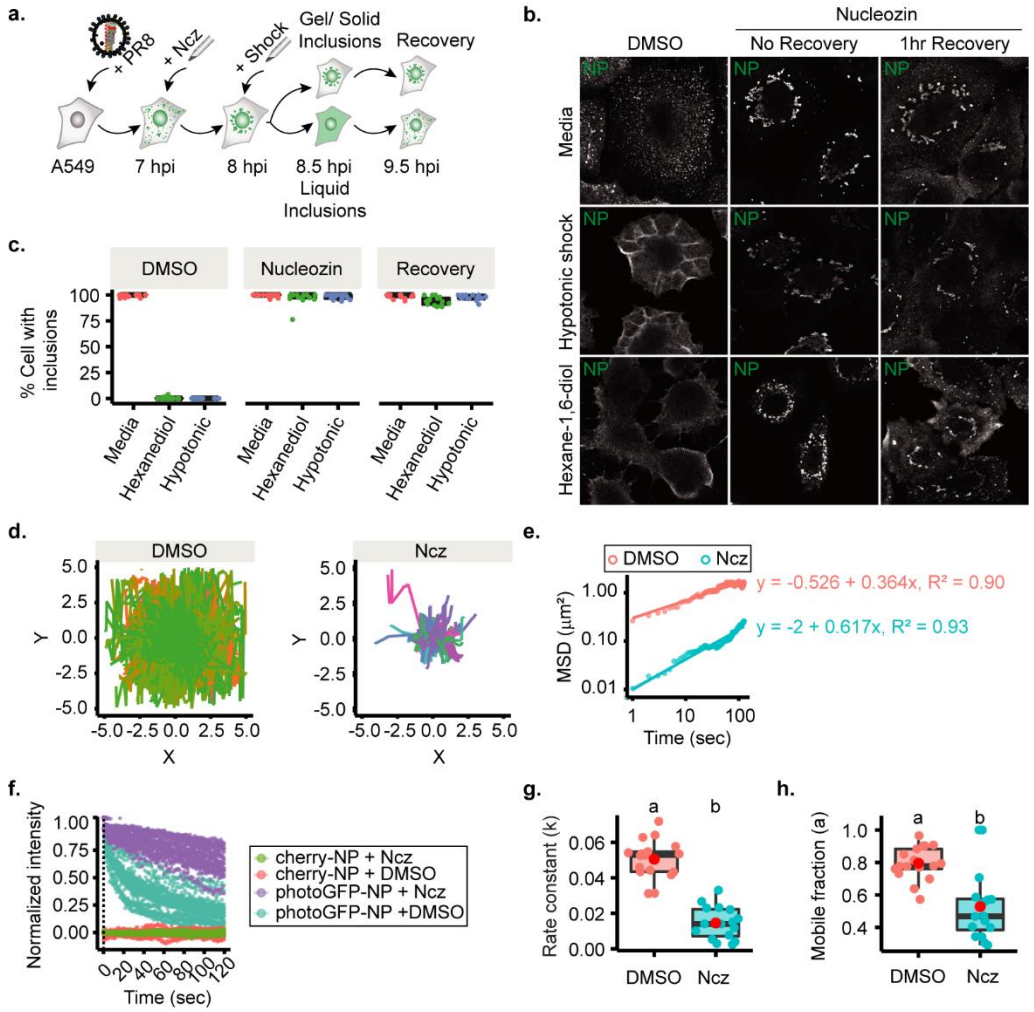

Extended Data Fig. 4: Hardened IAV inclusions are rigid, immobile, and irresponsive to shock. (a. - c.) A549 cells were infected at a multiplicity of infection (MOI) of 3 with PR8 virus, treated with 5 µM nucleozin (Ncz) or DMSO at 7hpi. An hour later, cells were treated for 30 min with 80% water (hypotonic shock, Hyp), with 1,6-hexanediol (Hex) or complete media (CM) as control. **a.** schematics of experimental setup **b.** Fixed immunofluorescence image showing IAV inclusions (NP, as proxy) response to shock treatments after incubation in 5µM nucleozin or DMSO. **c.** boxplot showing percentage cells with inclusions with or without nucleozin (Ncz) after manual scoring. P = 0; Kruskal Wallis Bonferroni treatment. **d. – h.** A549 cells were transfected with plasmids encoding either GFP-NP (**d. - e.**) or photoactivatable GFP-NP (**f. – h.**), co-infected with PR8 virus at an MOI of 10 and treated at with nucleozin (ncz) or sham vehicle (DMSO) at 12 hpi for onwards subsequent live imaging. **d.** Plot showing inclusion (GFP-NP, as proxy) particle trajectory when treated with DMSO or nucleozin (Ncz) **e.** Graph showing the mean square displacement (µm^2) versus time (sec) of IAV inclusions (NP, as proxy) in the presence or absence of nucleozin (Ncz). **f.** Dot plot showing every data point of normalized fluorescence intensity decay of photoactivated IAV inclusions. Coloured lines are single exponential model fitting ($y_0 = (1-a) + ae^{-kt}$) of the data point, dots are the mean of the data per second, and vertical lines denote the standard deviation (SD)

per time (sec). **g.** Decay constant (sec^{-1}) of DMSO and nucleozin treated inclusions. *P* = 1.386e-6; Kruskal Wallis Bonferroni treatment. **h.** Mobile fraction of DMSO- or nucleozin (Ncz)- treated inclusions. *P* = 0.000475; Kruskal Wallis Bonferroni treatment. Above each boxplot, same letters indicate no significant difference between them, while different letters indicate a statistical significance at α = 0.05.

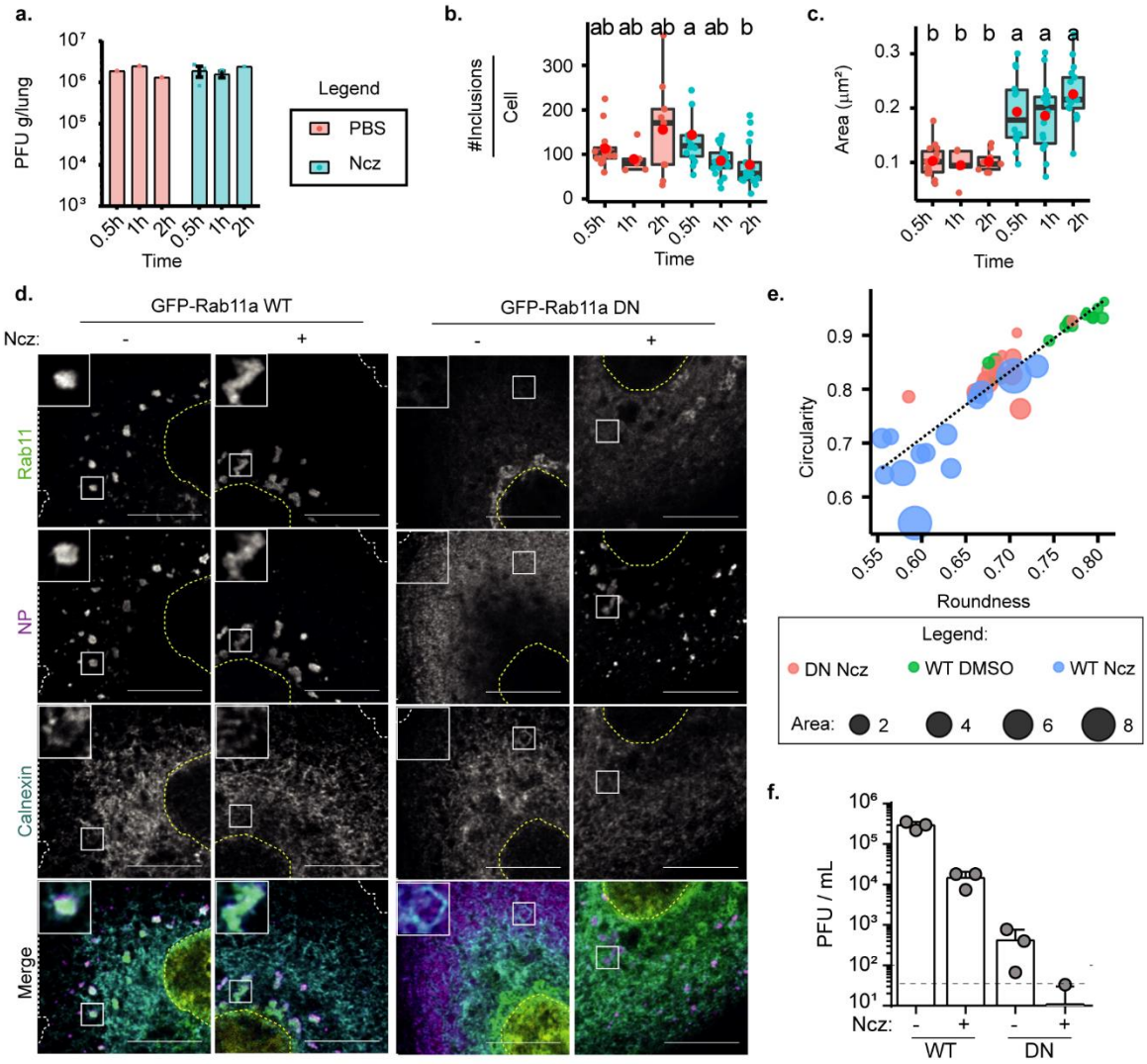

Extended Data Fig. 5: Only hardened inclusions emerge in nucleozin-treated Rab11a-DN cell line and *in vivo* infection. (**a. – c.**) Mice were intranasally infected with 4000 plaque forming units (PFU) of X31 virus, and after 2 days were intraperitoneally injected with PBS or 69 µg of nucleozin (Ncz) at 30 min, 1h or 2h before the collection of the lungs. **a.** Bar chart of viral titre (PFU g/ Lung) of mice after infection with X31 and treatment with PBS or Ncz. Data in (**b. - c.**) were extracted from segmented inclusions (NP, as proxy) from fixed immunofluorescence images of lung tissues. **b.** Boxplot showing the number of inclusions per cell in lung sections; P = 0.01399; Kruskal Wallis Bonferroni treatment. **c.** Boxplot showing the area (µm^2) of inclusions from cells in lung sections. P = 3.378e-8; Kruskal Wallis Bonferroni treatment. (**d. – f.**) A549 cells constitutively expressing GFP-Rab11a-WT and GFP-Rab11a-DN were mock- or PR8-infected for 12h and thereafter, treated with Ncz or sham vehicle-DMSO. **d.** Immunofluorescence images of inclusions (NP - magenta, Rab11 – green) and ER (Calnexin - cyan). Nuclei and cell periphery delimited by yellow and white dash line respectively, and white boxed are insets showing presence or absence of inclusions. Scale bar = 10 µm. **e.** Scatter plot of circularity versus roundness of inclusions. Above each

boxplot, same letters indicate no significant difference between groups while different letters indicate a statistical significance at α < 0.05. **f.** Bar chart showing viral titre (PFU/ mL). Experiments were done in twice with triplicate samples.

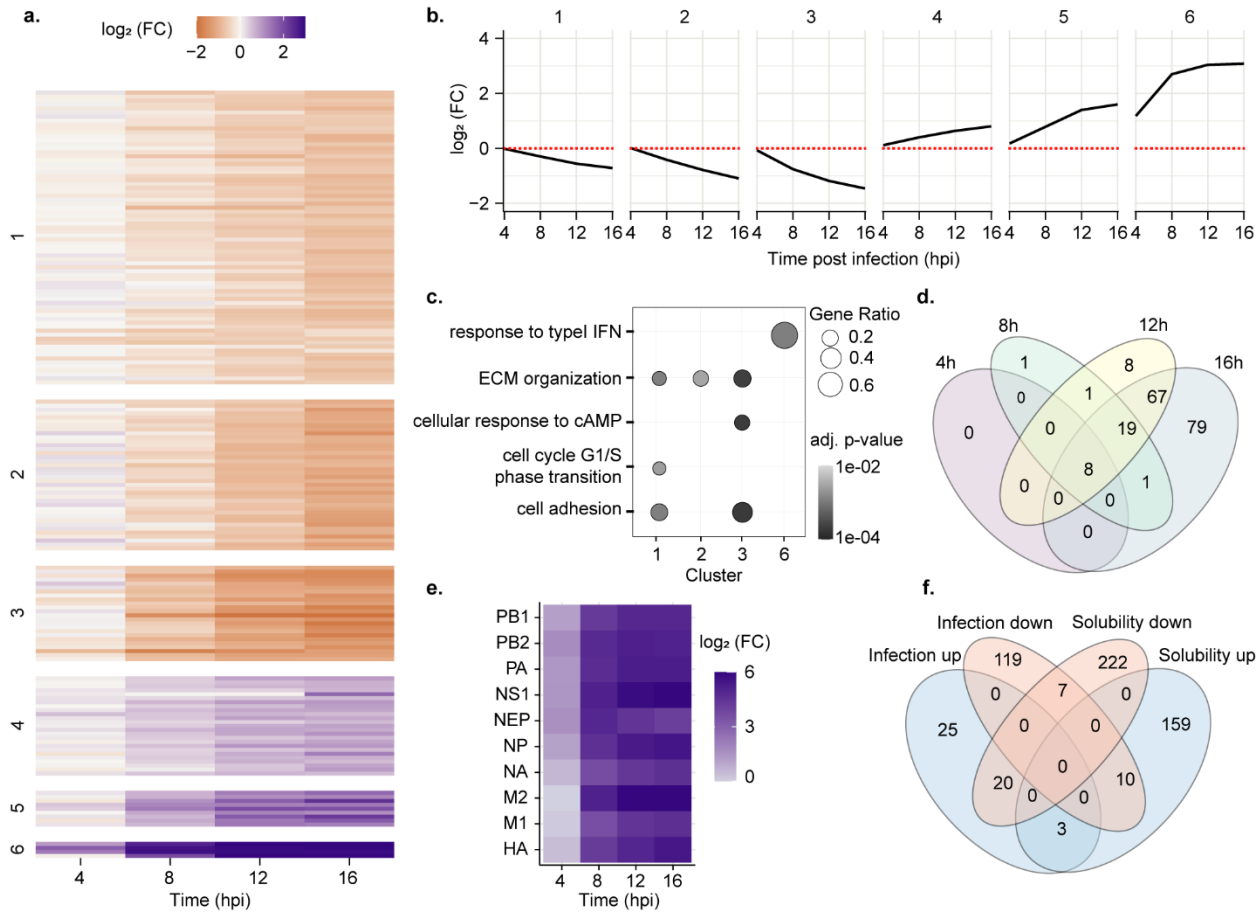

Extended Data Fig. 6: Proteome-wide abundance and solubility changes of host and influenza proteins. A549 cells were mock-infected for 12 hours or PR8 infected for 4, 8, 12 & 16 hours at a multiplicity of infection (MOI) of 5. Thereafter, cells were lysed in mild (NP40) or strong detergent (SDS), while NP40 lysate was ultracentrifuged (100,000 g) to pellet materials in condensates from the soluble fraction in the supernatant. Soluble and total host and viral proteome were identified by LC-MS/MS and solubility was determined as the ratio of soluble NP40- to SDS- derived total proteome abundances at the indicated hour post infection (hpi). **a.** Hierarchically clustered heat map showing relative abundance of host proteome along the indicated time course of infection in comparison to mock infection. Host proteins that are significantly (*see methods)* altered in abundance within any of the assayed time points were clustered to 6 distinct clusters based on the Euclidean distance. **b.** Line plot representing the median relative abundance (log_2 fold change, with respect to mock infection) of host proteins from 6 distinct clusters (shown in panel a) over the assayed time course of infection. Red dotted line shows unchanged log_2(FC) at 0 (values above

and below zero are more and less abundant respectively). **c.** Dot plots representing the gene ontology (GO) with terms of biological processes overrepresented among significant hits from proteome-wide abundance (shown in panel a). The dot size corresponds to the ratio of genes per cluster that belong to the indicated biological process, and the grey fill shows the adjusted p-value. **d.** Venn diagram showing sets of proteins from the relative host proteome abundance at different infection time. **e.** Heat map showing changes in median relative abundance (in log2 scale) of the PR8 influenza proteome along time of infection. **f.** Venn diagram of infection-solubility interaction in host proteome at different infection time.

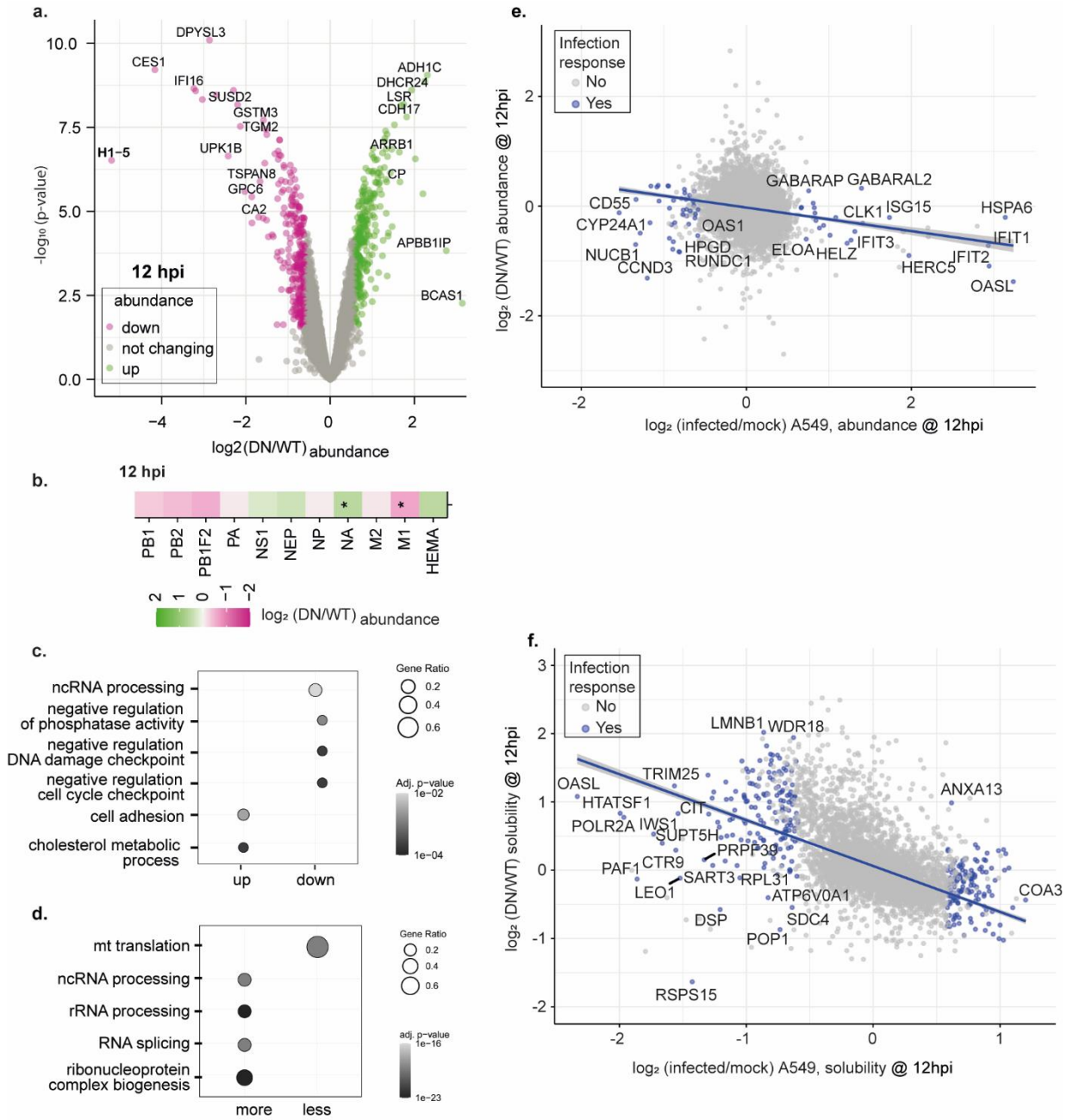

Extended Data Fig. 7: Changes in host proteome abundance and solubility in Rab11a-DN and Rab11a-WT infected cells. Cell lines constitutively expressing GFP-Rab11a-WT and GFP-Rab11a-DN; were infected for 12 hrs with PR8 at a multiplicity of infection (MOI) of 5. Thereafter, cells were lysed in mild (NP40) or strong detergent (SDS), while NP40 lysate was ultracentrifuged (100,000 g) to pellet materials in condensates from the soluble fraction in the supernatant. Soluble and total host and viral proteome were identified by LC-MS/MS and solubility was determined as the ratio of soluble NP40- to SDS- derived total proteome abundances at the indicated hour post infection (hpi). **a.** Volcano plot representing the differential abundance of host proteins in 12hpi infected Rab11a-DN cell line compared to Rab11a-WT line. High and low abundance proteins are represented in green and magenta dots respectively. **b.** Heat map showing changes in median relative abundance (in log2 scale) of the influenza proteome at 12hpi in Rab11a-DN cell line compared to Rab11a-WT line. High abundance and low abundance proteins are represented in green and magenta colours respectively. **c.** Dot plots representing the gene ontology (GO) with terms of biological processes overrepresented among significant hits from proteome-wide upregulated and downregulated proteins at 12hpi in Rab11a-DN cell line compared to Rab11a-WT line. The grey fill represents the adjusted p-value. **d.** Dot plots representing the gene ontology (GO) with terms of biological processes overrepresented among significant hits from proteome-wide differentially soluble proteins at 12hpi in Rab11a-DN cell line compared to Rab11a-WT line. The grey fill shows the adjusted p-value. **e.** Scatter plot comparing the relative changes in host protein abundance in 12 h infected Rab11a-DN with respect to Rab11a-WT (y-axis) versus changes in host protein abundance in 12 h infected A549 with respect to mock infection in $\log_2$ scale. Blue dots represent proteins with significant infection response in Rab11a-DN versus Rab11a-WT cell lines at 12 hpi. **f.** Scatter plot comparing the relative changes in host protein solubility in infected Rab11a-DN with respect to Rab11a-WT (y-axis) versus changes in host protein solubility in infected A549 with respect to mock infection, scaled to $\log_2$. Blue dots represent proteins with significant solubility response at 12hpi infection in Rab11a-DN versus Rab11a-WT cell lines.